Realization and Lateral Stable Workspace Analysis of an Axially Symmetric Scalable Hexapod Robot

by

Long Qu

A Thesis

Submitted to the Faculty

of the

WORCESTER POLYTECHNIC INSTITUTE

In partial fulfillment of the requirements for the

Degree of Master of Science

in

Mechanical Engineering

September 2013

APPROVED:

Professor Stephen S. Nestinger, Major Thesis Advisor

Professor Gregory S. Fischer, Graduate Committee Member

Professor Cagdas D. Onal, Graduate Committee Member

Professor John Blandino, Graduate Committee Representive

Abstract

The maintenance and inspection of societal structures and equipment such as skyscrapers, bridges, and ship hulls are important to maintaining a safe lifestyle. Improper maintanance and delayed inspection can lead to catastrophic failure. In lieu of placing humans in potential harm, mobile robotic machining systems can be used to enable remote repair and maintenance within constrictive, hazardous, and inaccessible environments. Due to their intrinsic high mobility and 6-DOF control, hexapod walking robots are a salient solution to mobile machining. However, the static structure of traditional hexapod robots can be rather limiting when attempting to traverse over irregular terrain or manipulating objects. This research realizes a new scalable hexapod robot and analyzes the lateral stable workspace of the robot under different external loading conditions. The scalable design allows the robot to extend its legs which enhances the workspace and improves stability while manuevering through constrictive and irregular terrain. The design incorporates two additional prismatic joints into the legs of the traditional hexapod robot design providing a compact, rigid, and efficient design. The electronic printed circuit boards were designed and assembled in-house. A distributed control architecture was implemented to off-load low-level leg control to dedicated leg controllers. An analysis on the lateral stable workspace of the scalable hexapod robot under different external loading conditions is presented. A dynamic stable workspace criterion is derived. The stable workspace criterion provides a metric for comparing stable workspaces between hexapod robots with different configurations. Multiple simulations and physical experiments were conducted to demonstrate the advantages of a scalability in hexapod designs.

Acknowledgements

First of all, I would like to extend my sincere gratitude to my academic advisor, Prof. Stephen S. Nestinger. He gives me a lot of useful advices on my project and flexible management, which makes me enjoy my years very much.

I would also like to thank all ME faculties and professors, who give me much help of my academic life.

I feel grateful to my roommates, who give me help a lot on my life. When I'm frustrate, they, especially Haowen Su, always enlighten me to continue my trip with even more confidence.

In these years, I owe much to my parents and other families. As an old Chinese saying goes, the homesick feeling will be stronger during the traditional festival. I feel guilty that I cannot be with them when family members should be together at all festivals, all days and nights. But they gave me the chance to study abroad, or I would be an ordinary graduate without any knowledge of outside world.

Last but the most important, I would like to give my most sincere gratitude to my best friends, who are now still fighting all around the world. Special thanks to Shuaihua Chen and Yi Lin, who teach me electronic design and answer my uncountable beginner's questions. Thanks to Zisu Huang, Junting Tan, Xuecong Pan, Beibei Ren, Zhihang Hu and Shihao Du, who are always with me and save me when I'm lost lonely and helpless. It is said, the place is your destination where the men who miss you are. Without their memories, I will have no destination to go.

The same thing as my undergraduate thesis:

With the immature answer I keep seeking in the past two years, finally, present to all the hope of future as a gift.

Contents

List of Figures

Chapter 1

Introduction

The maintenance and inspection of societal structures and equipment such as skyscrapers, bridges, and ship hulls are important to maintaining a safe lifestyle [1, 2]. Improper maintenance and delayed inspection can lead to catastrophic failure. Due to the confined and highly irregular environmental nature of these structures, routine maintenance and inspection can be rather tedious. Generally, these locations suffer from the lack of ventilated air creating a hazard for human workers especially when operating dangerous repair equipment that generate particulates. In lieu of placing humans in potential harm, mobile robotic machining systems can be used to enable remote repair and maintenance within constrictive, hazardous, and inaccessible environments. Mobile machining systems require the use of a mobile platform with attached tooling. In some circumstances, such as highly constrained environments with irregular surfaces, a mobile platform with high mobility and maneuverability is required. Due to their intrinsic high mobility and 6-DOF control, hexapod walking robots are a salient solution to mobile machining [3].

Traditional hexapod robots, such as the Lynxmotion hexapod robot [4] shown in Figure 1.1, are generally constructed using six 3DOF articulated legs connected to a main platform. However, the static structure of the traditional hexapod robot, can

Figure 1.1: A Lynxmotion hexapod robot [4]
(Source: RobotShop Distribution inc. ©2011)

be rather limiting when attempting to traverse over irregular terrain or manipulating objects. With a static structure, the robot may not be able to negotiate dynamic irregular environments while maintaining stability and orientation. In some scenarios,the robot may need to climb steps [2], cross large gaps [5] or go through small passage ways for pipe inspection [6]. The solution of long limbs for navigating large obstacles or crossing gaps contradicts with navigating small passage ways. Hence, having a scalable design would provide a flexible solution for navigating dynamic irregular environments.

This research presents a new scalable hexapod robot design to enhance the workspace and analyzes the lateral stable workspace of the robot under different external loading conditions. The scalable design allows the robot to extend its legs which enhances the workspace and improves stability while manuevering through constrictive and irregular terrain. The design incorporates two additional prismatic joints into the legs of the traditional hexapod robot design providing a compact, rigid, and efficient design. The design of the electronic printed circuit boards are presented in-house. A distributed control architecture was implemented to off-load low-level leg control to dedicated leg controllers. An analysis on the lateral stable workspace of the scalable hexapod robot under different external loading conditions is provided. A dynamic stable workspace criterion is developed to provide a metric for comparing stable workspaces between hexapod robots with different configurations. Multiple simulations and physical experiments were conducted to demonstrate the advantages of the scalability of the new hexapod design.

1.1 Thesis Contribution

The contributions of this research are as the follows:

- The design and fabrication of a new scalable hexapod robot is presented. The scalability of the design enhances traditional hexapod robot designs by incorporating two prismatic joints, an additional 2DOF, into each leg. Prismatic joints were selected to provide a high collapsable ratio with low torque requirements. The scalable hexapod robot is manufactured using a rapid prototype machine. Detailed component design and hardware selection is discussed.

- The design and fabrication of the electrical system and distributed control architecture for the scalable hexapod robot are presented. Each electronic printed circuit board was customed designed and assembled in-house. A distributed control architecture was developed to off-load low-level leg control to dedicated leg controllers.

- An analysis on the lateral stability and workspace of axially symmetric hexapod robots is completed. The analysis was conducted under different external stimuli to simulate a machining tool operation.

- A dynamic criterion is developed to integrate the concepts of robot stability and constant orientation workspace into a lateral stable workspace of an axially symmetric hexapod robot. The stable workspace criterion utilizes the Foot Force Stability Margin. The analytical solution of the lateral stable workspace is presented along with a metric for comparing stable workspace between different robot configurations. The lateral stable workspace of the scalable hexapod robot is analyzed, demonstrating the advantages of introducing scalability into the hexapod robot design.

- Simulated and experimental results are presented that demonstrate the workspace enhancement and flexibility of the scalable hexapod robot.

1.2 Thesis Organization

The rest of the thesis is organized as follows. Chapter 2 gives the details of robot mechanical structure design and the electronic system design, including parts selection, control strategy and actual control process. Chapter 3 analyzes the lateral workspace and stability of a hexapod and develops an algorithm of combination of lateral workspace and stability. Chapter 4 gives an analysis of lateral stable workspace on scalable hexapod robot and experimental demonstrations of the models and hardware developed in previous chapters, including simulation of stable workspace and robot machining experiment. Chapter 5 analyzes the results of simulations and experiments, which summarizes the advantages and disadvantages of the models and robot design. It also lists valuable points in future work. Chapter 6 concludes the thesis.

Chapter 2

Design and Fabrication of a Scalable Hexapod Robot

2.1 Mechanical Design

As discussed in the first chapter, there are several specifics which should be included in mechanical design. The robot should have the ability to traverse over irregular terrain and navigate through small passage ways. Thus, it should have long legs and a small overall size. To satisfy both requirements, a scalable structure is needed which provides a variable size external structure. The robot should be capable of carrying tools or additional devices. It is designed to satisfy some basic machining task with selected brushless motor. In the following sections, the weight of robot with the certain materials is considered. All robot parts size is based on the motor, which is the only drive part.

2.1.1 Scalable Structure

To realize the enhanced stable workspace, the robot is designed to have a scalable structure to achieve a flexible workspace. The key parameters which determines the

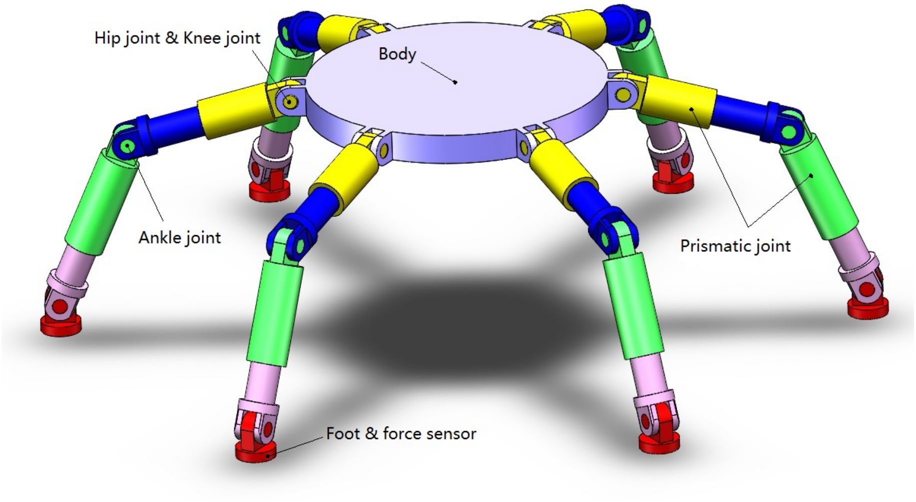

Figure 2.1: A 3D rendering a scalable hexapod

workspace of a robot are the leg lengths. If the leg lengths are variable, the workspace of the robot would not be fixed. Thus, to fit the design of a scalable structure, the most direct and simple way is to change the leg lengths. There are some optional rotation joint designs could be chosen to realize the similar requirements, such like folding rotatory joint. However, it may cause some accidents during working, like interference between the limbs. Thus, the prismatic joint is an more effective choice to realize the enhanced stable workspace.

Figure 2.1 shows a 3D rendering of a scalable hexapod robot using prismatic joints. Each leg has 5 active joints, including 2 prismatic joints with 2DOF for extension of the leg length and 3 rotation joints with 3DOF. The legs have corresponding feet connected by a passive joint. Each foot has a force sensor to measure ground contact forces.

Based on the scalable hexapod robot concept, a scalable hexapod robot was designed using Solidworks$^{\text{TM}}$ [7]. Figure 2.2 shows the CAD assembly of the designed scalable hexapod robot. The following sections discuss component design and hardware selection.

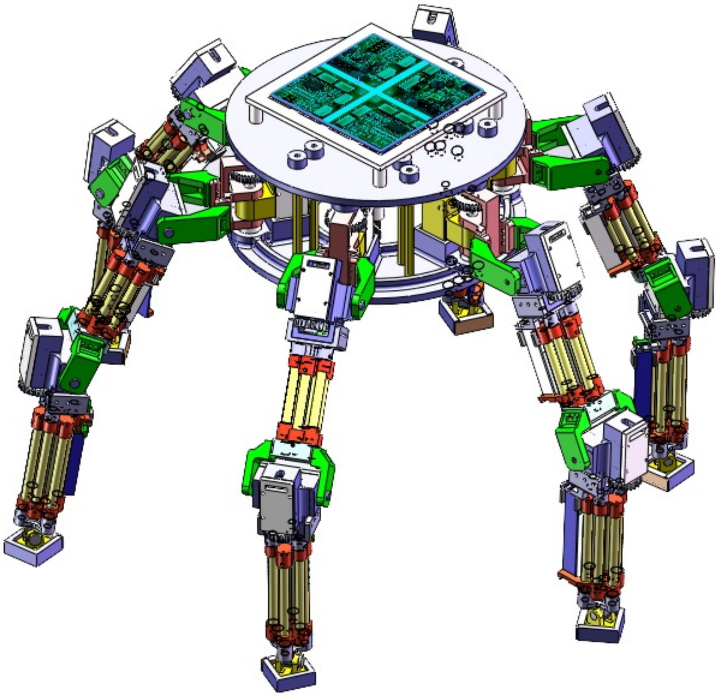

Figure 2.2: CAD assembly of the scalable hexapod robot design

2.1.2 Leg Design

The leg components were manufactured using ABS plastic through a rapid prototype machine. Figure 2.3 shows the assembled leg. The leg design incorporates a

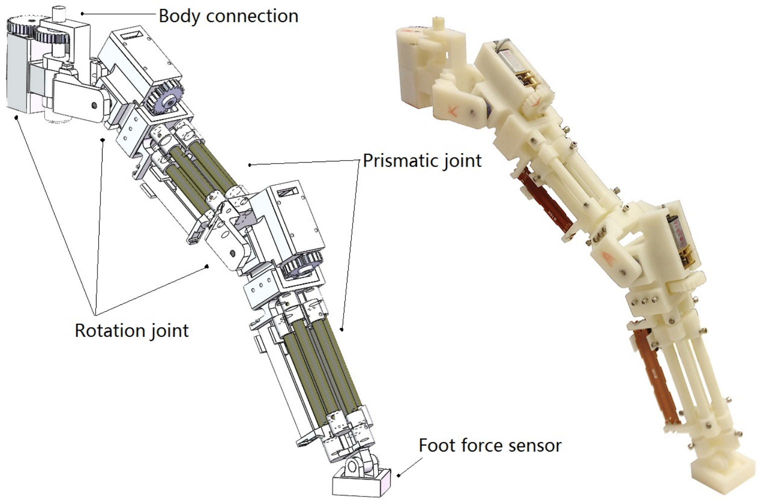

Figure 2.3: Assembled leg

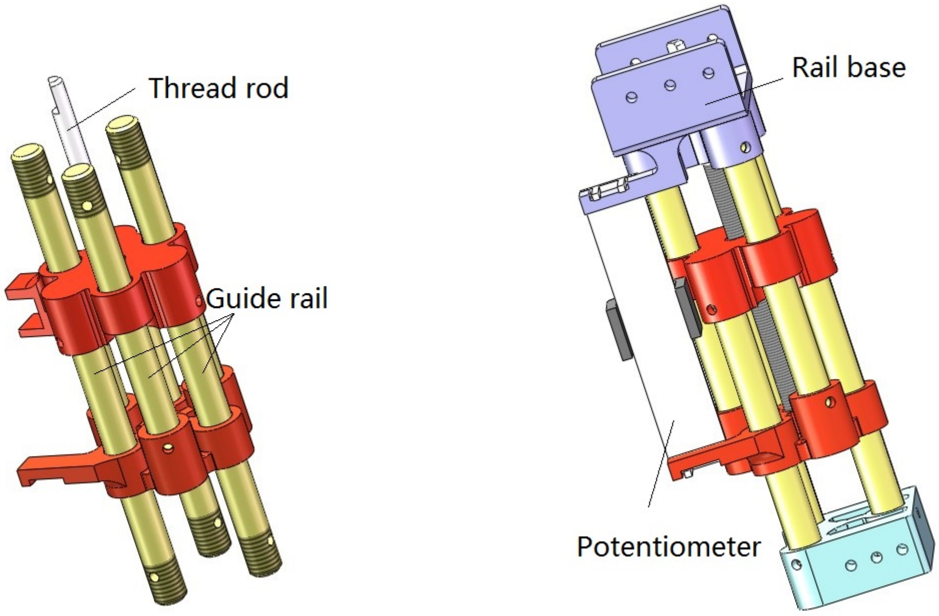

(a) Prismatic joint structure (b) Assembled joint

Figure 2.4: Prismatic Joint

body connection, three rotation joints, two prismatic joints and a foot force sensor.

Table 2.1 shows the actual designed ranges of motion of all 5 joints on the leg.

Prismatic Joint

The prismatic joints design provide used for linear motion for the extension of the leg. The design of the prismatic joint is shown in Figure 2.4. Figure 2.4(a) shows the threaded rod and guide rails. Figure 2.4(b) shows a fully assembled prismatic joint. To maintain rigidity throughout the motion of the prismatic joint, a triangular arrangement of three cylinders are used as the guide rails. A threaded rod is placed in the middle as the driving component. The six guide cylinders, which are mutually

Table 2.1: Range of joint motion

Lower leg extension	0 - 45mm
Ankle	0° - 110°
Upper leg extension	0 - 30mm
Knee	-10° - 110°
Hip	±30°

inserted, surround the threaded rod. The cylinders are fixed by relevant bases. There is also an additional slot for a linear potentiometer, which is used for measuring the linear motion and placed parallel to the prismatic joint. The stroke of the prismatic joint is 30mm for the upper leg part and 45mm for the lower leg part.

As is previously mentioned, the prismatic joint is driven by a the threaded rod. The rod is driven by a motor parallel to the threaded rod. The threaded rod driving motor placemente is shown in Figure 2.5. The motor and threaded rod are connected by a group of meshing spur gears. The transmission ratio of the spur gears is 1:1. Since the speed of rotation and provided torque have been considered during the motor selection, there was no need to adjust the RPM and torque output via gearing.

Hip and Knee Joint Designs

The hip and knee joints are two connection joint on each leg. One of the two rotation joints is connecting two prismatic joints, the other one is connecting the leg and body (body connection joint). Since each part of leg has one motor for extension and one motor for rotation, there are two motors on each part of leg. To shorten the length of leg, the two motors are placed compactly. The power output of rotation is perpendicular to extension, therefore the two motors' position are are the shape of a cross.

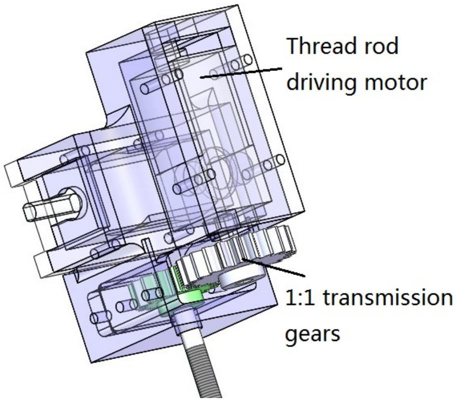

Figure 2.5: Parallel driving structure for thread rod

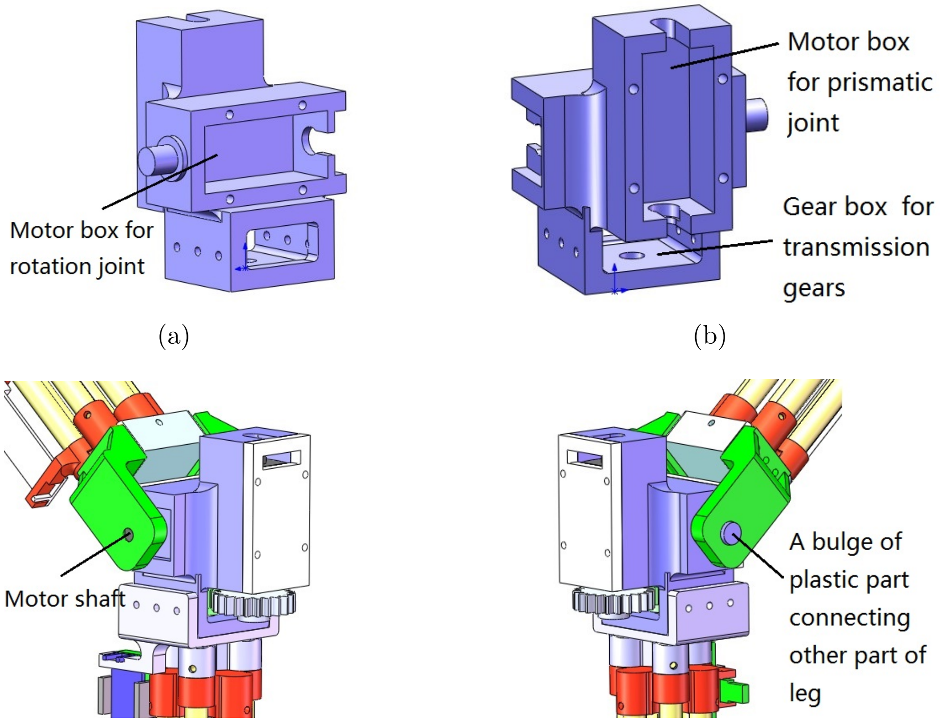

(a) (b) (c) (d)

Figure 2.6: Rotation Joint

Figure 2.6(a) shows the motor box for the rotation motor. Figure 2.6(b) shows the other side of the joint, which is the motor box for the extension motor. The box under the two motor would contain a gear connecting to the threaded rod. Figure 2.6(c) shows the driving side of the rotation joint. The pivot is the shaft of the motor, connecting to another part directly. Between the gear box of motor and external plastic connection part, there is position sensor on the motor shaft. Figure 2.6(d) is the connection side of the joint. The pivot of connection side is a bulge of joint part, constructing the axle together with the shaft of motor.

Body Connection

The body connection joint couples the legs and body platform. One motor is involved this joint. Due to the limited length of the motor shaft, the shaft could not be used as the axle of the connection joint. Hence, another axle with a parallel power driving structure was used. The parallel axle design for the body connection is shown

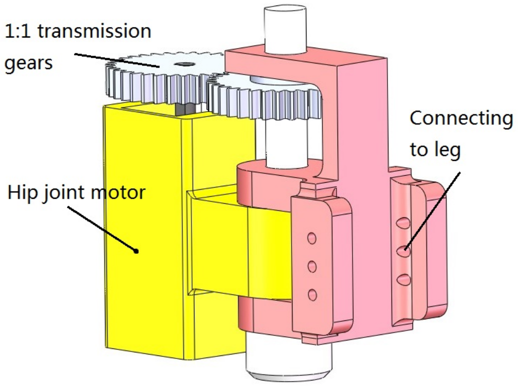

Figure 2.7: Body connection joint

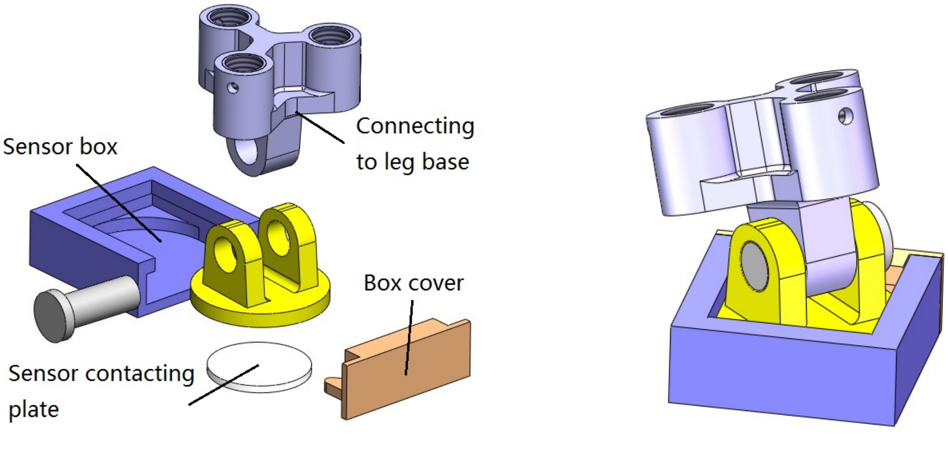

(a) Exploded view (b) Assembled view

Figure 2.8: Foot force sensor box

in Figure 2.7. The transmission ratio of the spur gears is 1:1.

Foot Force Sensor

The foot force sensor is included in an enclosure box as shown in Figure 2.8, which as act the feet of the robot. The enclosure was designed to fit a force resistance sensor shown, to measure ground contact forces. Figure 2.8(a) shows an exploded view of the foot force sensor enclosure. The enclosure contains a sensor box and cover, a sensor contacting plate, a connector to the leg and an axle connecting to the base. This structure has 2-DOF. Although it is possible to rapid prototype a ball joint, it is hard to assemble the plastic parts and the plastic lacks a smooth surface.

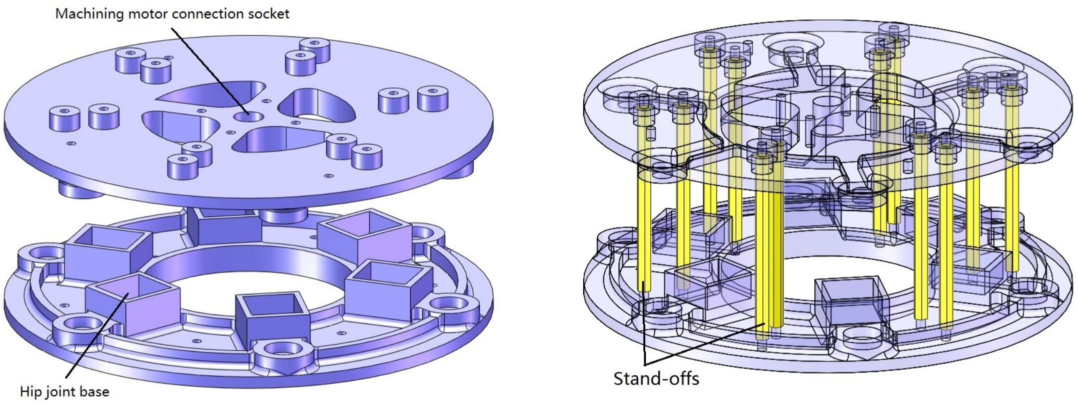

(a) (b)

Figure 2.9: Robot body platform

2.1.3 Body Platform Design

The body platform of the robot connects to six legs, a brushless motor for machining and carries the control boards. The body is built using a top and bottom, and twelve stand-offs. On the bottom plate, there are six bases for leg connections plate. Six features are placed around the body with equal distance. Both the top and bottom plates have bearings for the rotational axles. At the center of the top plate, there is a socket for connecting a brushless motor. Figure 2.9(a) shows the two plates. Twelve stand-offs symmetrically located about the main axis of robot as shown in Figure 2.9(b).

2.1.4 Mechanical Hardware Selection

The weight of the whole robot is estimated between 1kg and 1.5kg. Each leg will be between 100g and 150g. Considering some additional equipments connected to robot body or legs, the motor which shoulders the largest load should be able to handle the load of 200g or more. Thus, the selection of motor is chosen 250g as its regular load standard. Traditional hexapod robots utilize servo motors due to ease in control. However, servo motors with sufficient torque requirements can be rather

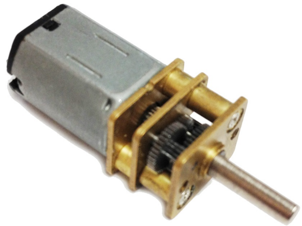

Figure 2.10: A Pololu 298:1 Metal Gearmotor HP [8]
(Source: Pololu Corp. ©2011)

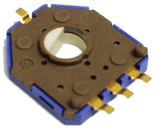

Figure 2.11: Rotation potentiometer [9]
(Source: Murata Manufacturing co., ltd ©2009)

expensive. Due to the required number of motors for the scalable hexapod robot design, compact DC motors were used.

The Pololu metal gearmotor [8] was selected as the DC motor of choice. This gearmotor, as shown in Figure 2.10, is a miniature (0.94" x 0.39" x 0.47"), high-power brushed DC motor with 298:1 metal gearbox. A metal gear box provides better longevity compared to a gear box made of plastic. The Pololu gearmotor has a 0.365"-long, 3 mm-diameter D-shaped output shaft. The motor rotatesat 100 RPM at 6V, requires 70mA in free-run and has a stall current of 1.6A [8]. It provides 70oz/in (5kg/cm) of power output, which is more than enough to handle the estimated weight of the leg.

A 10kΩ rotational potentiometer [9] is capable of fitting the 3mm motor shaft, as shown in Figure 2.11, was selected as the rotational position sensor. It works at the same voltage as the logic circuit.

A force resistance sensor [10] is selected for the foot force sensor. The foot force sensor varies its resistance depending on how much pressure is being applied to the sensing area. It can sense an applied force within the range of 100g to 10kg.

The brushless motor connecting to external machining tool uses the type shown in Figure 2.13. The NTM Prop Drive 35-36A 910 brushless motor [11] was selected for the machining motor. It is rated at 910kv with a no load current of 1.6A The brushless motor is controlled with an EXCEED-RC VOLCANO/PROTON Series

Figure 2.12: Force sensor [10]
(Source: SparkFun Electronics ©2010)

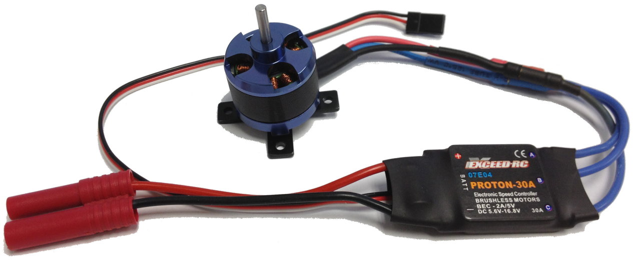

Figure 2.13: Brushless motor [11, 12]
(Source: EXCEEDRC.COM ©2012)

Figure 2.14: Linear motion sensor [13]
(Source: BI Technologies Corp ©2009)

Brushless Electronic Speed Controller [12].

The position of the prismatic joints is measured using a slide potentiometer [13] shown in Figure 2.14 . The working condition is similar to the rotational potentiometer. To reduce the weight of leg, the external cover will be removed before being assembled onto the robot leg.

A #4-40 threaded rod was selected, as the lead screw for the prismatic joint. With 40 threads per inch and a gear motor output of 100RPM, the leg should extended at 0.042 inches per second (1.6mm/s).

Slotted #4-40 pan head screws were selected to connect the stand-offs to the body. A stand-off with the same thread size of #4-40 and length of 2.5in was used as the support between the body plates.

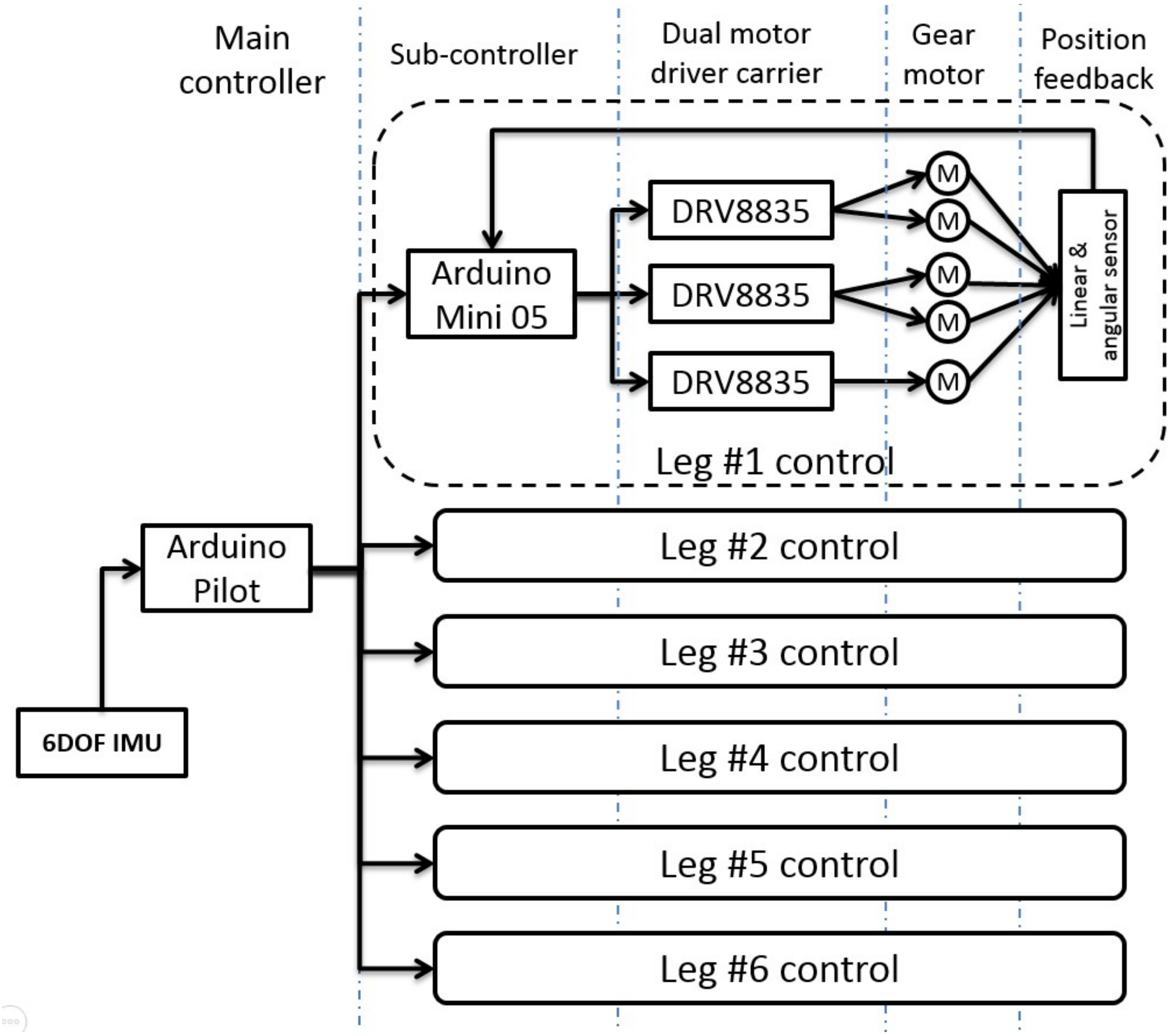

Figure 2.15: Control architecture of the scalable hexapod robot

2.2 Electronic and Control System Design

Figure 2.15 shows the control architecture of scalable hexapod robot. A distributed control architecture is used to relieve computational load from the main controller. Each leg has a dedicated controller for position control which handles the low-level leg control loop. With a distributed control architecture, The main controller is free to handle full robot pose control while passing leg positions to the leg controllers.

2.2.1 Electronic Hardware Selection

An Arduino Pilot [14], shown in Figure 2.16(a), was selected as the main controller. It has an Atmel mega1280 processor, both digital and analog inputs and outputs, and PWM outputs. It also supports multiple peripheral communication protocols.

The sub-controller is an Arduino Pro mini (5V/16MHz) [15] with an ATmega328 processor, as shown in Figure 2.16(b). There are 6 sub-controllers in the system.

The Pololu DRV8835 Dual Motor Driver Carrier [16], shown in Figure 2.16(c), was selected as the motor driver for the legs. The driver can deliver 1.2A per channel continuously (1.5A peak) to a pair of DC motors and it supports two possible control interfaces for added flexibility of use. The driver has an operating voltage range from 2 to 11 V and built-in protection against reverse-voltage, under-voltage, over-current, and over-temperature [16].

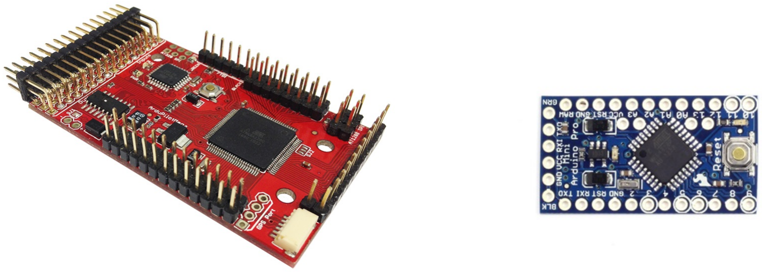

(a) Arduino Pilot board
(Source: SparkFun Electronics ©2010)

(b) Arduino Pro mini board
(Source: Sparkfun Electronics ©2012)

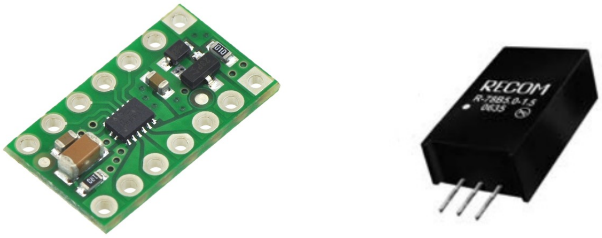

(c) Motor driver
(Source: Pololu Corp.©2012)

(d) RECOM 5V switching power regulator
(RECOM Electronic ©2011)

Figure 2.16: Source: Electronic components

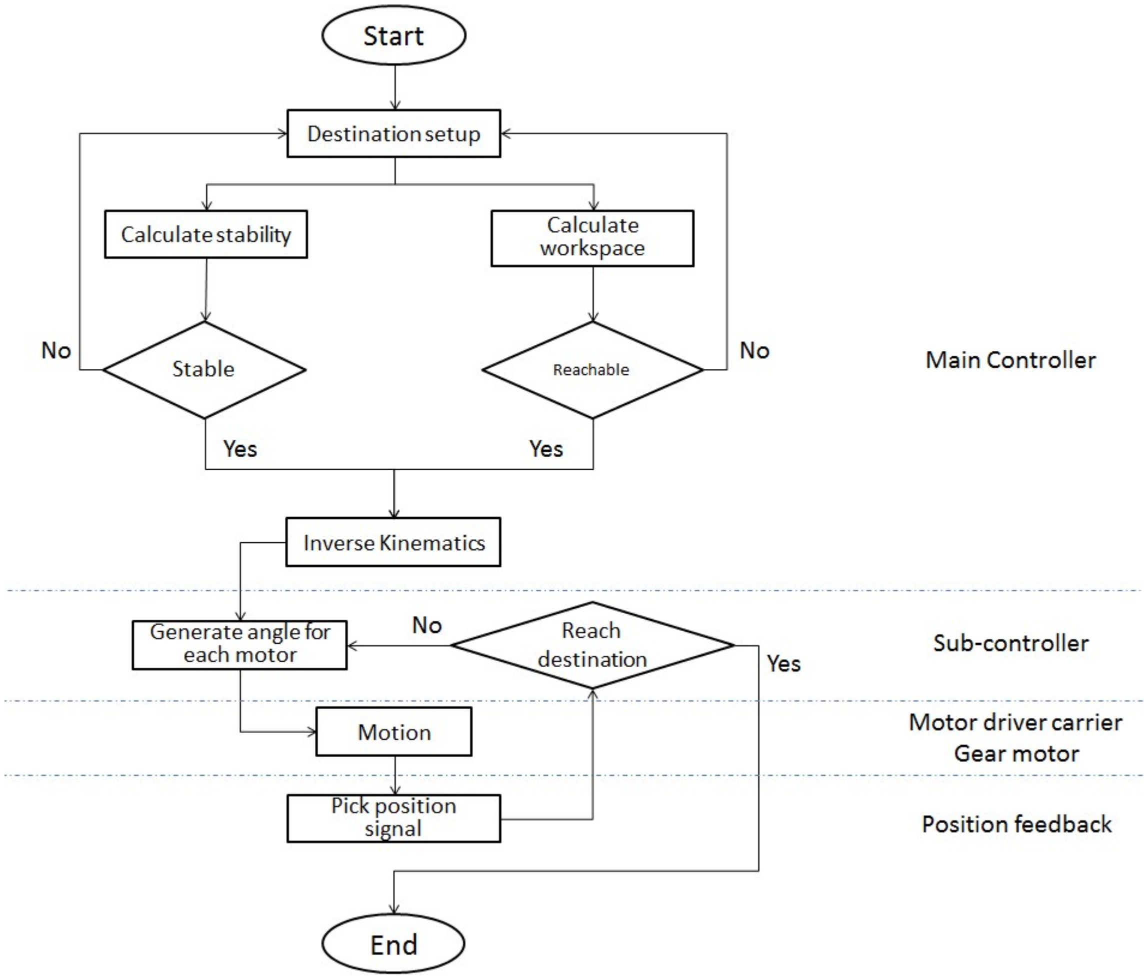

Figure 2.17: Control flow chart

Multiple voltage convertors were used to provide 5V for the electronics. A RECOM R-78B series DC/DC-Converter [17], as shown in Figure 2.16(d), was selected. It is a switch regulator which is more efficient than traditional linear regulators.

2.2.2 Control Algorithm and Flow

The control architecture of the stable hexapod robot is shown in Figure 2.15. The system is structured as a closed system with feedback. A flow chart is shown in Figure 2.17. It is easier to identify the relation between task of work and parts.

The initial command comes from remote terminals or has been pre-setup in main controller. The main controller, the Arduino Pilot, is responsible for receiving commands and generating high-level action decisions. The action of the whole platform is distributed to each leg by inverse kinematics calculation of input parameters and sent to each sub-controller by the end of each calculation. The main controller and sub-controllers are connected with the I^2C bus.

The action command will be sent transfer from the main controller to the sub-controllers. Each sub-controller is responsible for translating action information to motor signals, which move the joints to desired positions. The sub-controllers process the signals feedback and give feedback to main controller for further action decisions.

The motor driver is controlled by the sub-controller directly and is powered using a separate power supply circuit compared to the logical circuit. Each Arduino Pro mini can control 3 motor drivers and each driver can handle 2 motors. Technically, each driver group could carry 6 motors, though each leg has 5 motors and uses 5 channels of PWM output of sub-controller.

Linear and angular sensor would produce position signals after motion. The signal will return to sub-controller to see if the parts reach desired destination.

Single Leg Control

Figure 2.18 shows a leg control module, which is the drive module including sub-

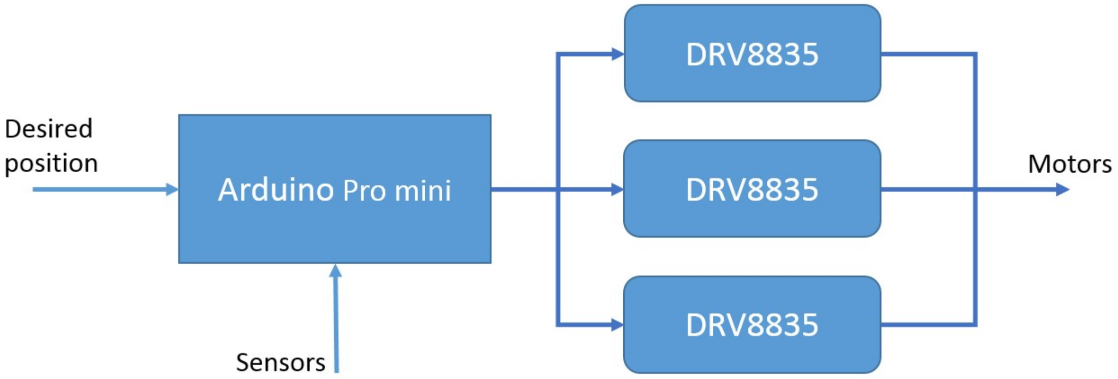

Figure 2.18: Sketch of single leg control

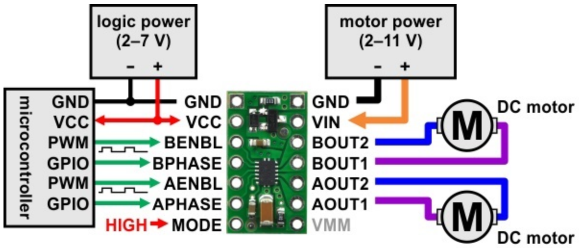

Figure 2.19: Wiring diagram of DRV8835 connecting environment [16]

Table 2.2: Simplified drive/brake operation with MODE=1 (PHASE/ENABLE) [16]

xPHASE	xENABLE	xOUT1	xOUT2	operating mode
1	PWM	L	PWM	reverse/brake at speed PWM%
0	PWM	PWM	L	forward/brake at speed PWM%
X	0	L	L	brake low (outputs shorted to ground)

controller and motor drivers. See Figure A.2 in Appendix A for the schematic of the drive module. The sub-controller has analog input to Arduino Pro mini as the position feedback. The sub-controller has 6 ports for analog input. The traces also contain some other connections to other functional module shown in the schematic, such as to logic circuit power supplement net, I^2C net and reset button net. The A4(SDA) and A5(SCL) pins are for I^2C communication.

There are three motor drivers for each one sub-controller. Figure 2.19 gives a wiring diagram for connecting a microcontroller to a DRV8835 dual motor driver carrier in phase-enable mode [16]. In consideration of the number of PWM outputs on a sub-controller, the motor drivers are placed in “PHASE/ENABLE” mode. On the sub-controller board, the IO ports of 3, 5, 6, 9, 10, 11 provide PWM outputs. They connect to the “ENABLE” ports of the motor drivers in sequence. The rest of the IO ports (2, 4, 7, 8, 12) are connected to the “PHASE” port of the DRV8835 providing GPIO output.

Figure 2.19 also shows that a motor driver has two groups of output ports connecting to motor. Each carrier handles two motors at most. There is also a trace net to keep motor driver at current work mode with high level. Power input to motor

```
while(joint position is away from destination)
  {
  Rotation direction command;
  Rotation speed commmand;
  Read current joint position;
  }
 Set the joint to keep current position;
```

Figure 2.20: Pseudo code for the motor controller

driver is from two different ways with different voltage. One is from voltage converter module with 5V, and the other is directly from battery with the same voltage of battery. Table 2.2 [16] is a truth table of the working conditions of motor driver carrier.

The motor driver is used as a on-off controller, or bang-bang control. The pseudo code in Figure 2.20 controls the ankle joint. If the angle difference from the current position to the destination is larger than the given value, the motor driver will set to output mode with one channel controls the rotation direction and the other controls the speed of rotation. After the joint reached the desired position, the motor driver will be set to low level to stay at current position.

2.2.3 Integrated Board Design

The initial control board used an integrated design with everything on a single board. Figure 2.21 shows the layout of the integrated board. See Figure A.1 in Appendix A for the schematic. From Figure 2.21, Arduino Pilot is at the center of the board. All communication with on-board chips is through external wires. Around the Arduino pilot are 6 leg control modules. On the right side are some related subfunction circuits, including logic circuit power output, sensor power supplement, net of reset button and voltage converter and distribution.

Figure 2.22 shows some other related subfunction circuits. In Figure 2.22(a) is a single row header which is 3 groups power output with voltage of 5V. It can satisfy

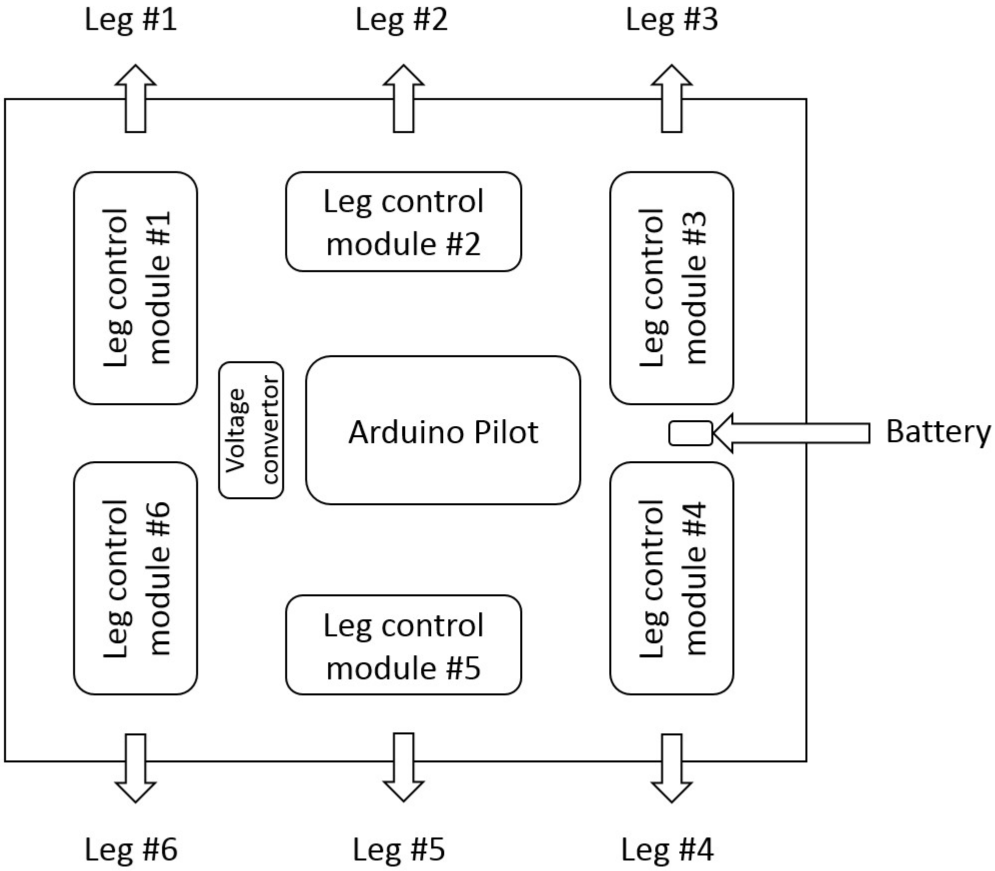

Figure 2.21: Integrated control board layout

the power requirement of the Arduino Pilot or some other additional accessories.

Figure 2.26(b) is the I^2C on-board connection. The double pins header connects the main controller with external wires. The right side traces connect to the sub-controllers. On the left is the power supplement of the I^2C bus with two voltage pull-up resistors at 4.7kΩ.

Figure 2.22(c) shows a local circuit providing power to the linear and rotational position sensors with the same voltage as the logic circuit net. It is divided into 6 ways corresponding to 6 legs. For each leg there is a 2 pins header.

Figure 2.22(c) shows the part of total power supplement. The current from the battery is divided into 3 parts. One is for motor energy usage with the same voltage as original input. One is to the R-78B5.0-1.5 which pulls the voltage down to 5.0V

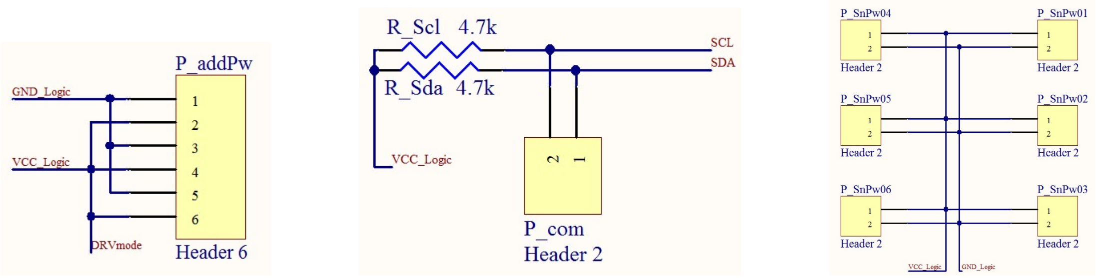

(a) Power output (b) I^{2}C connection (c) Sensor power supplement

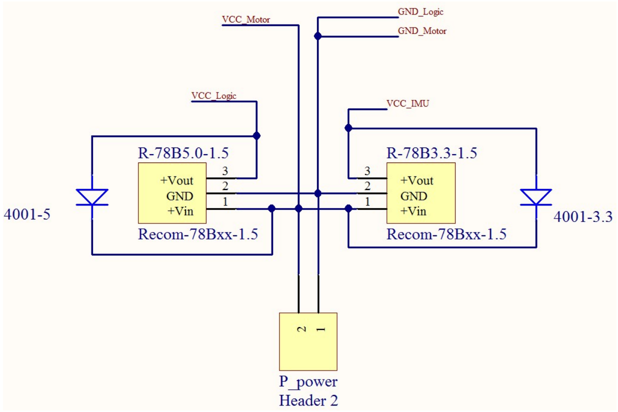

(d) Power division and variation of voltage

Figure 2.22: Related subfunction circuit

at a maximum current of 1.5A. The last one is to the R-78B3.3-1.5, which pulls the voltage to 3.3V. All of the branches use common ground. There is also a diode for each converter to prevent reverse current.

The PCB was designed for 4 layers. In consideration of the compactness of all parts on a 5x6in^2 board, power traces were limited to cross other traces and may fail to reach the required width for large currents. Among the 4 layers, 2 internal layers are used as power planes, to maximize the power transmission area.

Figure A.3 (in Appendix A) shows the PCB layout. Figure 2.23 shows the fabricated board.

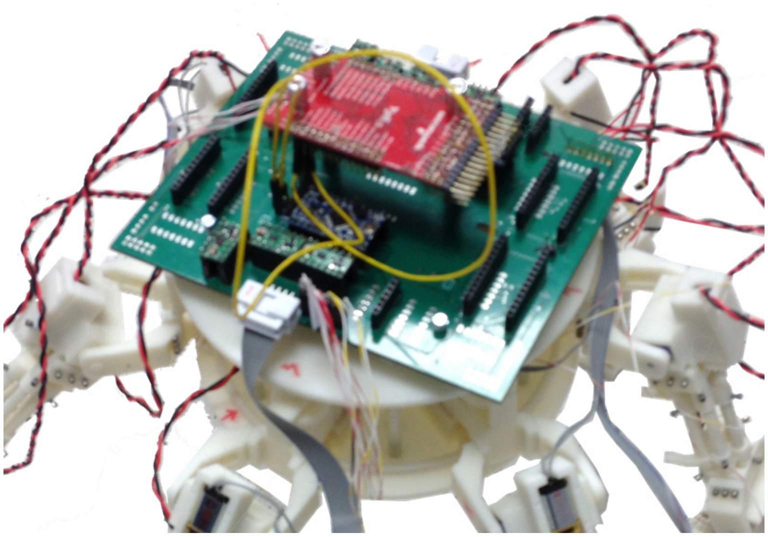

Figure 2.23: Integrated control board fabrication

2.2.4 Distributed Board Design

The integrated board design supported all of the desired functionality, but there were several drawbacks. The expense of manufacturing 4-layer boards is generally doubled and compared to 2-layer boards. Another drawback is, the modules of leg sets could not be fixed or replaced separately. If one module set on the board fails, it whole board needs to be replaced.

Due to the errors wit the manufacturing of the integrated board, a new PCB was designed. The new design uses distributed boards and divides the integrated board into modules. Related functional parts or chips are integrated onto separate boards. The whole system is more compact and the number of board layers was reduced to 2 layers. Figure 2.24 shows a layout of the distributed board system.

For board design distribution, each leg is controlled by one board with a sub-controller and 3 motor drivers. Hence, there are 6 leg boards in total. The boards are structured in parallel and connected to a central power board using the I^2C protocol. The Arduino Pilot and power supplement are both connected to the power board using external wires.

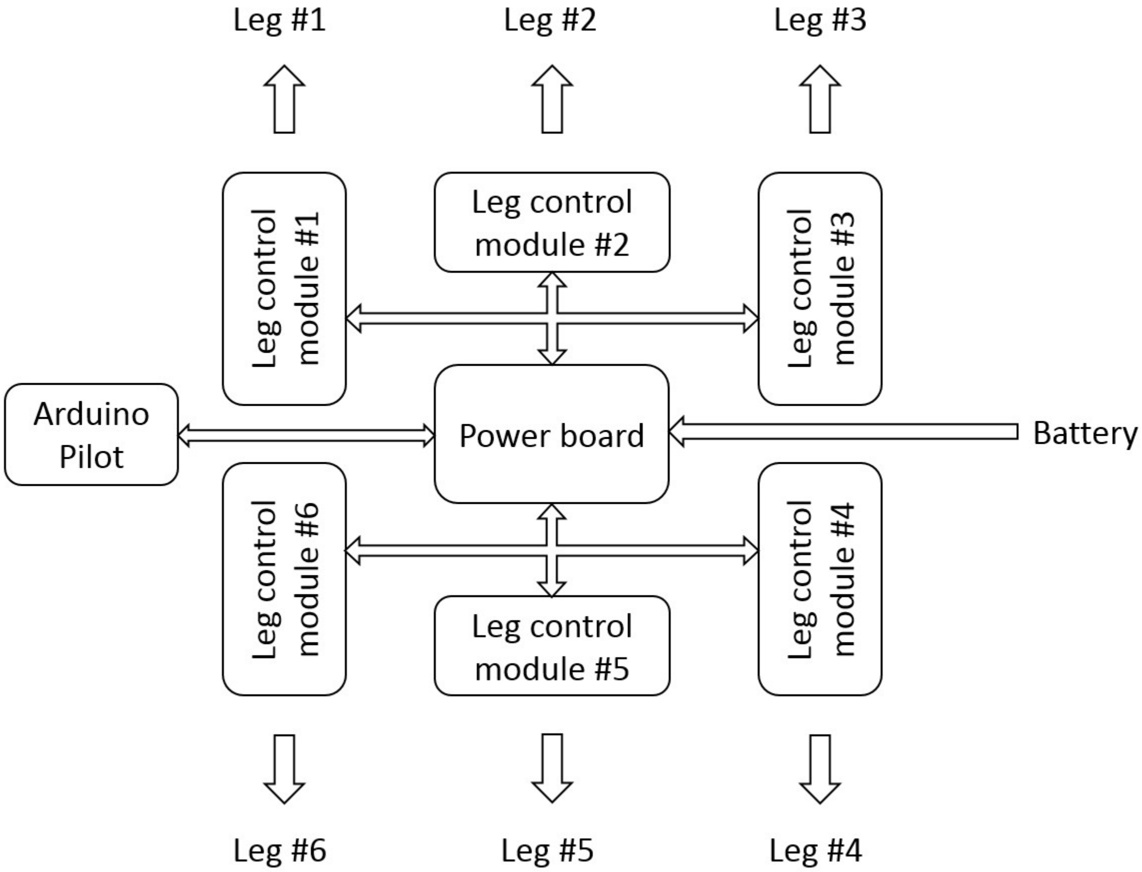

Figure 2.24: Distributed control board layout

On each leg board, there are 3 motor drivers responsible for 5 gear motors and grouped as 2-2-1, and 1 sub-controller to translate position orders to motor motion orders. Capacitors were added for rapid motor startup and for protecting the voltage convertor.

All part configurations are similar to the integrated generation. The leg boards only contain sub-controllers, motor drivers and related accessories. Other power related parts or modules are all placed on power board. The capacitors for rapid motor startup are connected in parallel to the motor drivers and voltage convertor. See Figure A.4 in Appendix A for the schematic of the controller leg board. There are 2 double rows headers with 10 pins on board. One is connected to the motors, the other one is used for connecting to the power board. Pins from 1 to 6 are power

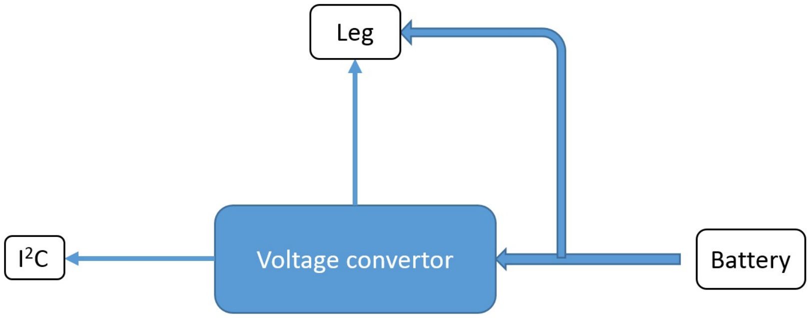

Figure 2.25: Sketch of distributed power board

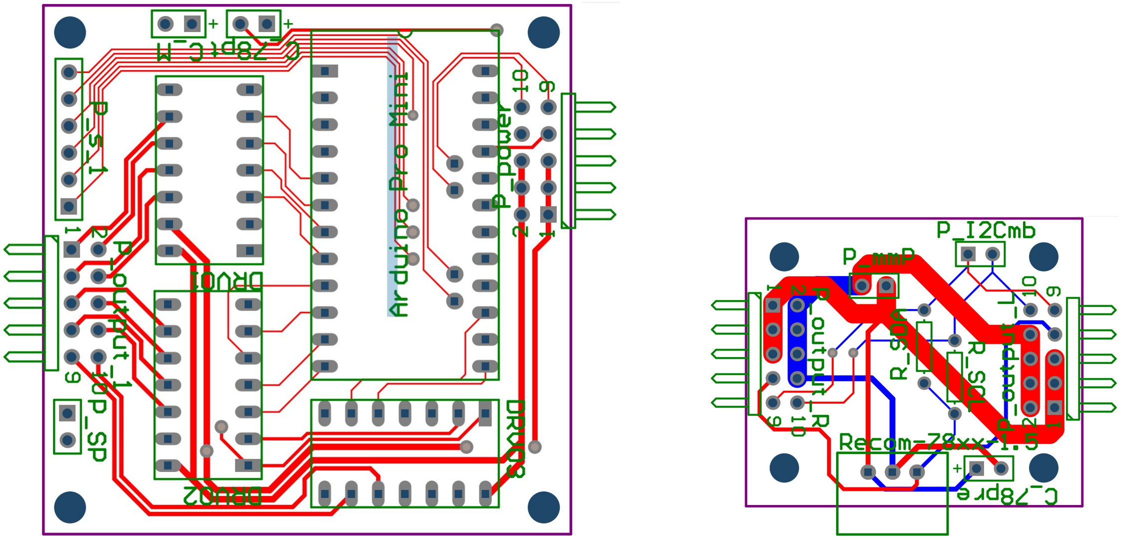

(a) Leg board

(b) Power board

Figure 2.26: PCB layout of distributed control board

supplement for the motor drivers. Six pins are used for power since the peak current cannot be handled by a single wire. Pins 7 and 8 power the logic circuit, which is connected to voltage convertor. Pins 9 and 10 are connected to the I^{2}C bus.

Figure 2.25 shows a flow layout of the power board. See Figure A.5 in Appendix A for the schematic of the power board. The power board has a voltage convertor on-board and pull-up resistors for the I^{2}C bus. The power board provides 6V to the leg boards (motor driver) and converts the input voltage to 5V for the logic circuits. A capacitor was added for protecting the voltage convertor. The power and bus are divided into 2 ways (2 double rows header with 10 pins) with 3 legs on each side, to

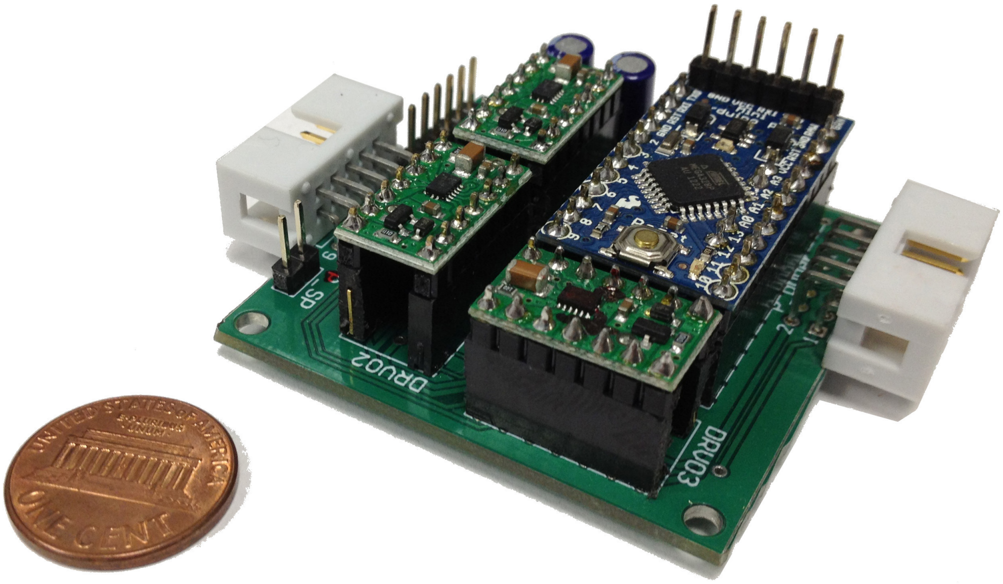

Figure 2.27: Assembled Leg board

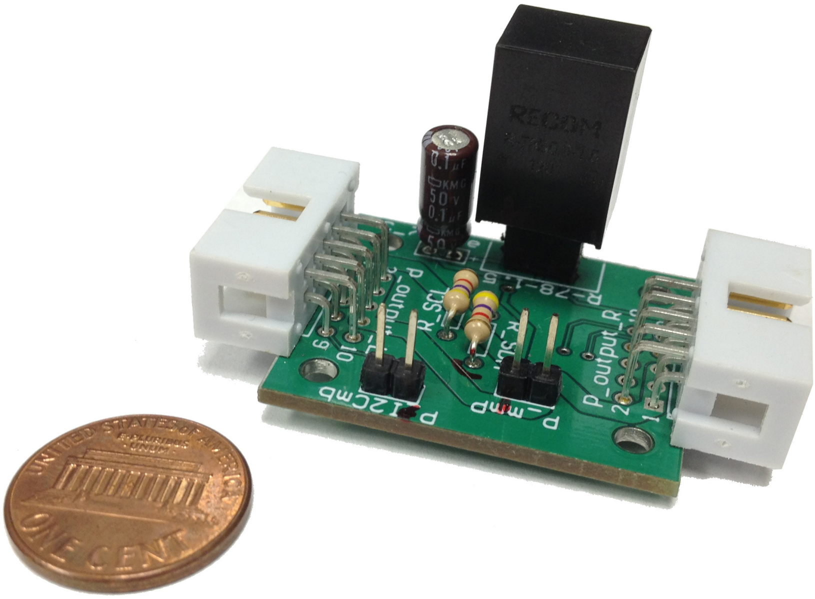

Figure 2.28: Assembled Power Boards

form a circuit transmission. 2 double pins header are for the I^2C connection to the main controller and external power input.

The distributed PCB board was fabricated with 2 layers. Figure 2.26 shows the layout of two boards. Figure 2.27 and Figure 2.28 show the two assembled boards.

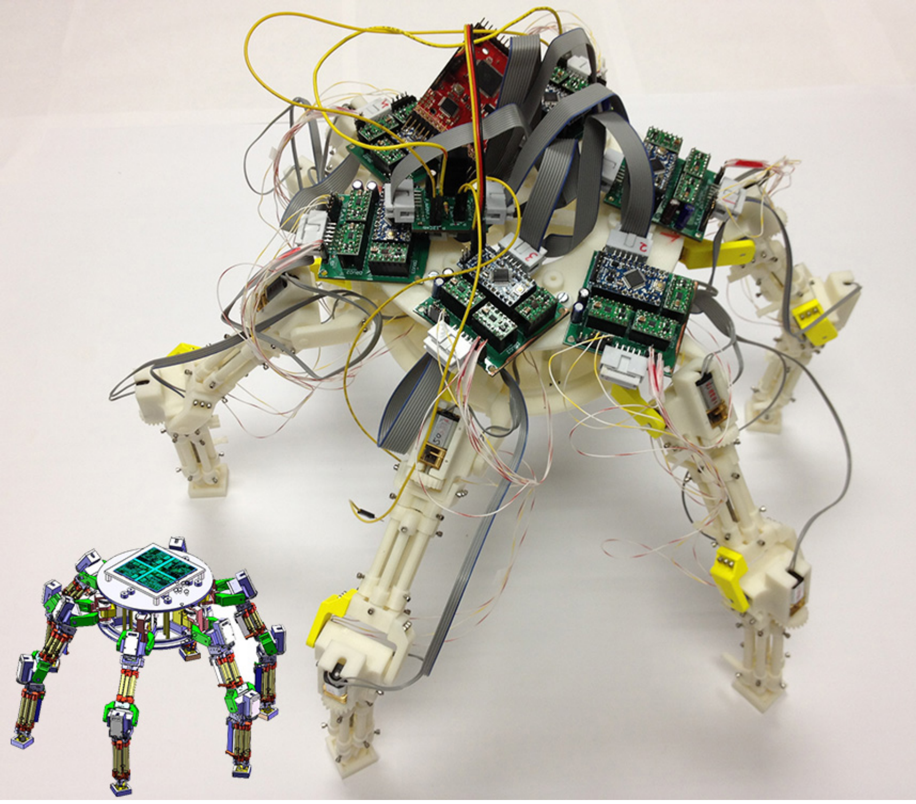

Figure 2.29: Fully assembled robot

2.3 Fabricated Scalable Hexapod Robot Prototype

Figure 2.29 shows the actual assembled robot, comparing to the design on lower left corner of the figure. Most parts are manufactured by rapid prototype machine. Figure 2.30 shows the details of the prismatic joint. Figure 2.31 shows a top-down view of fully assembled control system.

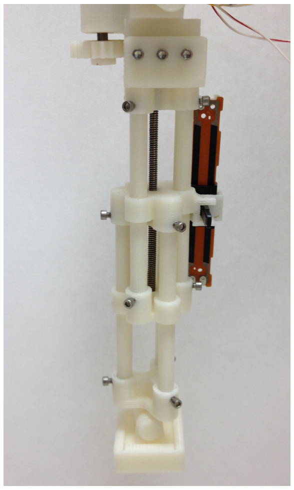

Figure 2.30: Details of prismatic joint

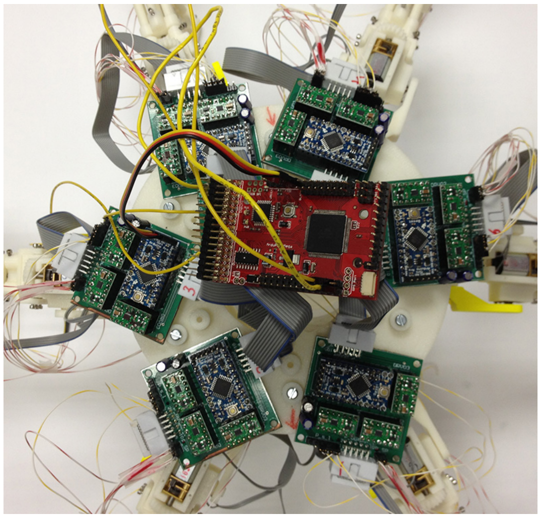

Figure 2.31: Partial view of electronics

Chapter 3

Lateral Stable Workspace Analysis

When attempting to execute a planar machining operation in the lateral plane of a hexapod robot, as depicted in Figure 3.1, the lateral tooling workspace becomes a key performance metric [18]. On the other hand, the robot should not tip over while operating within the lateral workspace. Focusing on the lateral plane, only the legs of the robot in the lateral plane are considered available for system stabilization. The out-of-plane legs may be occupied for walking and unable to contribute in the stabilization of the robot. Therefore, the stability and workspace integration problem in lateral machining using a hexapod robot can be reduced to a planar mechanism problem in which the articulated legs are virtually replaced with a prismatic joint as shown in Figure 3.2(a). Looking at the lateral plane and using the equivalent

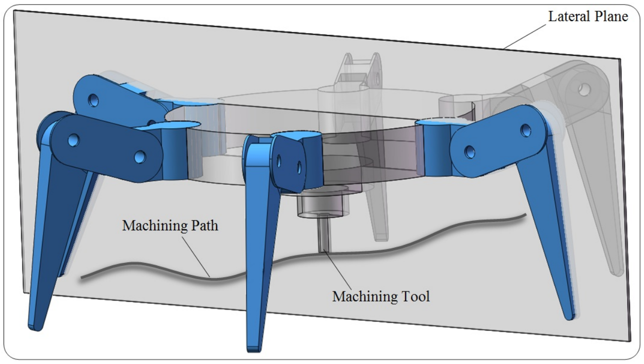

Figure 3.1: A hexapod robot performing a planar machining operation

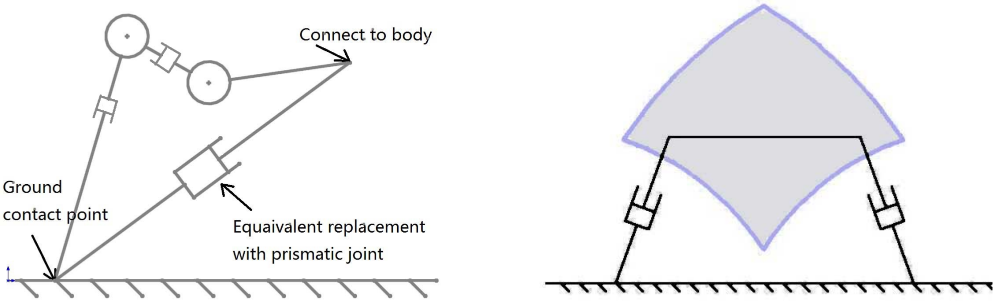

(a) Equivalent prismatic model of the robot leg

(b) Constant orientation workspace of the model

Figure 3.2: The equivalent robot model and workspace

prismatic model of the robot leg, the hexapod walking robot can be simplified to a 2-RPR planar parallel mechanism as shown in Figure 3.2(b), where the grey masked area is the constant orientation workspace of the model.

The workspace [18–28] and stability of planar parallel mechanisms have been previously studied independently. During the machining process, the robot may be stable at a desired position that is not within the workspace. Hence, the system would be stable but unable to complete the desired machining process. In some situations, the desired location may be reachable but not stable. Therefore, it is important to determine the stable workspace, defined as the specific subspaces of the workspace which are stable and reachable. This chapter solves for the stable workspace of 2-RPR parallel mechanisms by integrating stability into the workspace problem assuming the robot maintains a constant-orientation workspace [18]. Although any stability criteria may be used to derive the stable workspace of a given system, the presented derivations are based on the Foot Force Stability Margin(FFSM) [29].

3.1 Lateral Stable Workspace

There are separate models and criteria for workspace and stability. The algorithm for determining the stable workspace solves the stability problem within the workspace

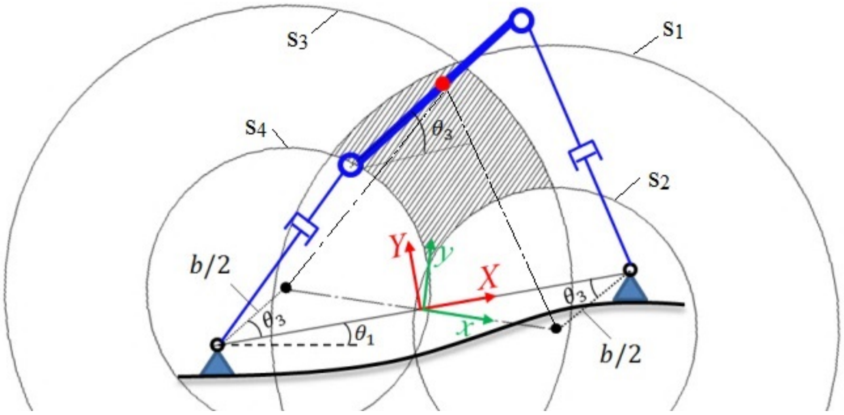

Figure 3.3: Size comparison of boards

model. The following sections describe the modeling of the workspace, the criterion for determining the stability of the system, and the algorithm for integrating both to find the stabile workspace of the system.

3.2 Workspace Modeling

The hatched area in Figure 3.3 is the constant orientation workspace of a 2-RPR parallel mechanism [18]. The following assumptions have been made with regards to the platform: the center of gravity of the system is at the center of the platform, the platform is horizontal, the system is on level ground, and the system has symmetric legs.

In the model shown in Figure 3.3, a horizontal platform and level ground is achieved when $\theta_1 = 0°$ and $\theta_3 = 0°$. Under these conditions, the boundary of the constant orientation workspace is the intersection of the circles s_1, s_2 s_3 and s_4. The equations for the circles is as follows:

$$\begin{aligned} s_1 &: (x+a)^2 + y^2 = L^2 \\ s_2 &: (x+a)^2 + y^2 = l^2 \\ s_3 &: (x-a)^2 + y^2 = L^2 \\ s_4 &: (x-a)^2 + y^2 = l^2 \end{aligned} \tag{3.1}$$

where L is the maximum permissible leg length, l is the minimum permissible leg length, and a = d/2 - b/2 where b is the dimension of platform and d is the distance between the two feet in contact with the ground.

3.3 Stability Criterion

Although any stability criterion may be used to determine the stability of the system, the presented derivations utilize the Foot Force Stability Margin (FFSM) [29]. The FFSM uses the normal foot force distribution of the system as the stability metric which is calculated using

$$S = FFSM = \frac{f_1 f_2 \cdots f_n}{\overline{f}^n} \quad 0 \leq S \leq 1 \tag{3.2}$$

where n is the number of supporting legs with non-negative normal foot forces, f_i is ith normal foot force and $\overline{f} = \frac{1}{n}\sum_{i=1}^{n} f_i$ is the average of all normal foot force magnitudes. In Eqn.(3.2), the foot force magnitude is always non-negative. When the foot force reaches zero, the corresponding foot has lost contact with the ground and the value of S becomes zero, indicating platform instability. When a foot force is positive, the foot force applied to the planar mechanism platform from the contact surface can be broken up into the normal component and the tangential or friction component, relative to the contact surface.

3.4 FFSM-Based Lateral Stability of Axially Symmetric Hexapod Robots

The free body diagram of the hexapod robot in the lateral plan and under external loads is shown in Figure 3.4. It is assumed that any external loads e.g. moments or forces from tooling or manipulation, can be translated to the CG of the robot by an equivalent moment and force. The external force F is decomposed into the horizontal and vertical components, F_x and F_y, respectively. The angle θ is the angle between the external force F and the gravitational direction. The components of the external force F are given by

$$\begin{aligned} F_x &= F\sin\theta \\ F_y &= F\cos\theta \end{aligned} \tag{3.3}$$

The distance between two fixed feet is represented by D. The forces F_x and F_y are the decomposition of the external force F. The moment M is the external moment. The force G is the force due to gravity. h is the height of the robot platform with respect to the ground. Assume all of the model structures are rigid, including the joints, and the system is static. The external forces act at CG, except the surface contact forces. All foot contacts are assumed to be point contact.

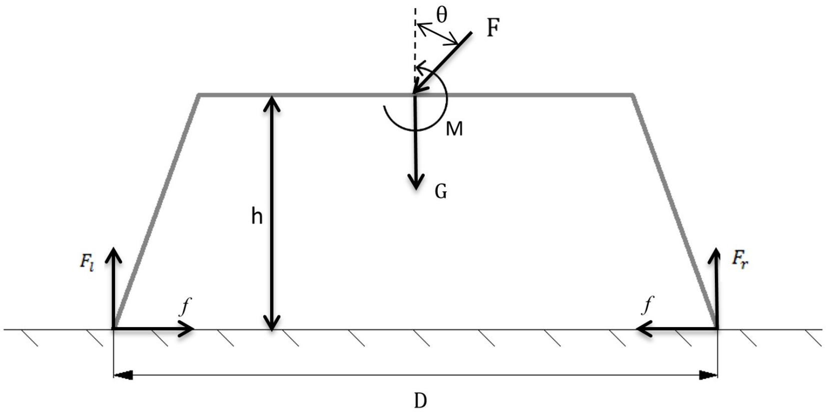

Figure 3.4: The free body diagram of the platform

Under static conditions, the equations governing the forces and moments in the system can be found by separately taking the moments about the two foot contacts. Eqn.(3.4a) is based on the moment balance around the left contact point and Eqn.(3.4b) is the moment balance about the right contact point.

$$F_x h - F_y\left(\frac{D}{2}+x\right) + M - \left(\frac{D}{2}+x\right)G + F_r \cdot D = 0 \tag{3.4a}$$

$$F_x h + F_y\left(\frac{D}{2}-x\right) + M - \left(\frac{D}{2}-x\right)G - F_l \cdot D = 0 \tag{3.4b}$$

In the Eqn.(3.4), x is the displacement of the CG. Solving for F_r and F_l, the analytical solutions for the foot force distribution is given by

$$\begin{aligned} F_r &= \tfrac{1}{D}\left(-F_x h + F_y\left(\tfrac{D}{2}+x\right) + \left(\tfrac{D}{2}+x\right)G - M\right) \\ F_l &= \tfrac{1}{D}\left(F_x h + F_y\left(\tfrac{D}{2}-x\right) + \left(\tfrac{D}{2}-x\right)G + M\right) \end{aligned} \tag{3.5}$$

Using FFSM, the stability of the robot is given by

$$S = FFSM = \frac{F_r F_l}{\left(\frac{F}{2}\right)^2} = 1 - \frac{\left(2M + 2yF_x - 2xF_y - 2xG\right)^2}{D^2\left(F_y + G\right)^2} \tag{3.6}$$

3.5 Effect of Stability on Workspace

An example is used to help in the discussion on the effects of stability on the workspace. The example assumes $D = 50$ cm, $G = 50$ N, and that the platform is on level ground. Figures 3.5(a)-3.5(h) overlap the stability margin lines with the constant orientation workspace of the platform given different external loading conditions. Figure 3.5(a) shows the robot in the home position with no external forces. Due to the symmetrical cross-section of the robot, the maximum stable working area is at the center of the workspace. Figure 3.5(b) shows the case in which only a clockwise moment is applied. Figure 3.5(c) shows an opposite moment applied compared to Figure 3.5(b). From Figure 3.5(b) and 3.5(c), the applied moment shifts the stability

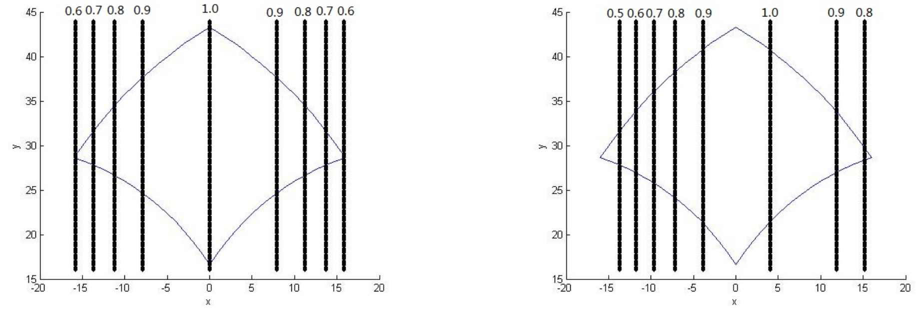

(a) $\theta = 0° \ F = 0N \ M = 0N \cdot mm$ (b) $\theta = 0° \ F = 0N \ M = 200N \cdot mm$

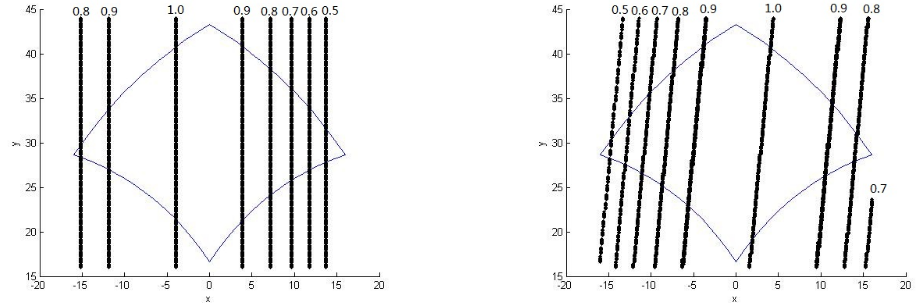

(c) $\theta = 0° \ F = 0N \ M = -200N \cdot mm$ (d) $\theta = 20° \ F = 20N \ M = 0N \cdot mm$

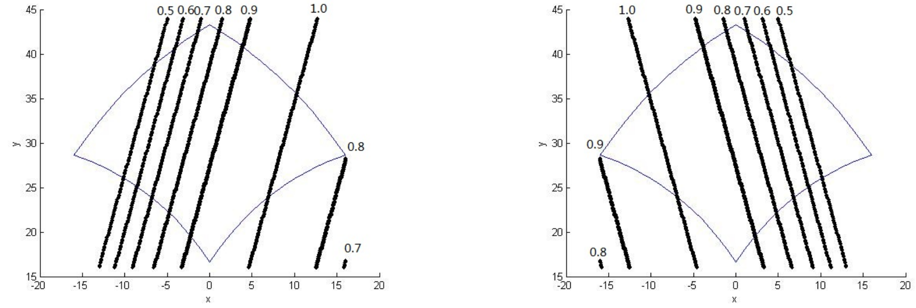

(e) $\theta = 60° \ F = 20N \ M = 0N \cdot mm$ (f) $\theta = -60° \ F = 20N \ M = 0N \cdot mm$

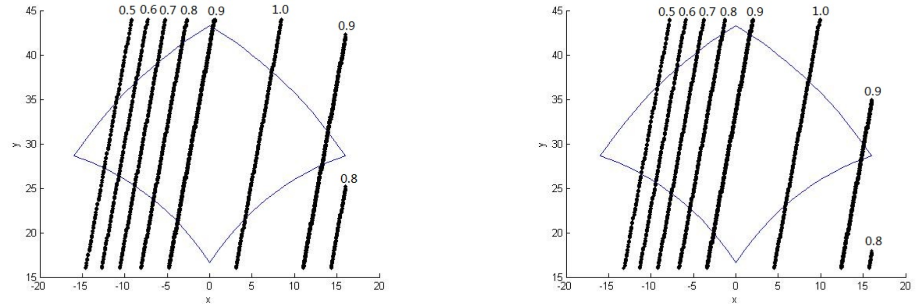

(g) $\theta = 20° \ F = 60N \ M = 0N \cdot mm$ (h) $\theta = 20° \ F = 60N \ M = 150N \cdot mm$

Figure 3.5: Overlapping stability margin lines with workspace

distribution horizontally. Figure 3.5(d), 3.5(e) and 3.5(f) give examples when only external forces are applied with various angles towards the robot platform. When an external linear force is applied to the system at an angle, the stability margin lines are rotated. The comparison between Figure 3.5(d) and 3.5(e) shows that the rotation and angle of the force relative to the transformation of the stability lines have a positive linear correlation. Figure 3.5(f) shows the effects of rotation transformation of the stability margin lines caused by changing the angle of the external force. Forces with a positive angle cause a clockwise rotation of stability margin lines. Figure 3.5(g) and 3.5(h) demonstrate the effect of having an external moment and load. The transformation of the stability margin lines in Figure 3.5(g) is a horizontal shift which proves that the effects caused by the external force and moment are independent of each other.

3.6 Stability Constrained Workspace

The extent of the stable workspace is defined by the desired maximum and minimum stability margin range. Given the desired stability margin range, the available workspace boundaries can be derived. Figures 3.6(a)-3.6(h) show the constrained workspace of the platform given a minimum allowable stability margin of 0.9 as an example to enclose a stable workspace area under different loading conditions. The grey area represents the stable workspace. In the last three figures, either none or a small fraction of the stable area overlaps the platform workspace. Figures 3.6(a)-3.6(h) demonstrate that under certain conditions, it is possible for the robot to be stable but unable to reach the desired location. When the stability area does not overlap with the platform workspace, the robot system is considered unstable under the given configuration of the platform and external loading conditions.

To evaluate if the desired platform CG location is within the stable workspace,

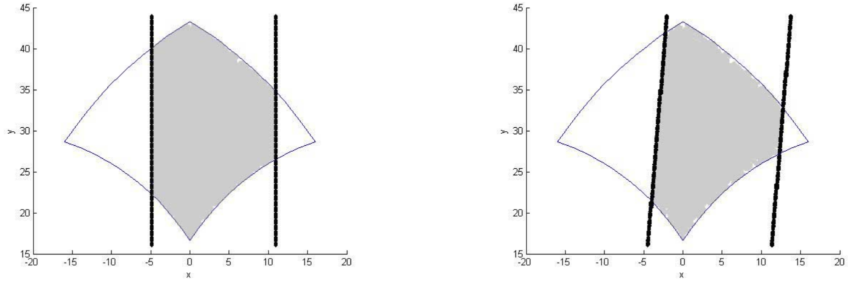

(a) $\theta = 0° \ F = 0N \ M = 200N \cdot mm$

(b) $\theta = 20° \ F = 20N \ M = 200N \cdot mm$

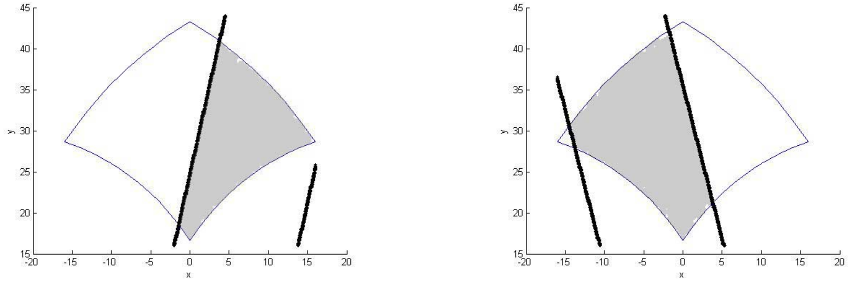

(c) $\theta = 60° \ F = 20N \ M = 0N \cdot mm$

(d) $\theta = -60° \ F = 40N \ M = 150N \cdot mm$

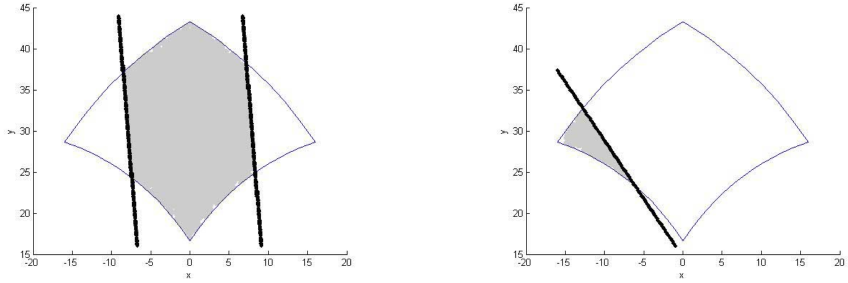

(e) $\theta = -20° \ F = 20N \ M = 0N \cdot mm$

(f) $\theta = -60° \ F = 60N \ M = 200N \cdot mm$

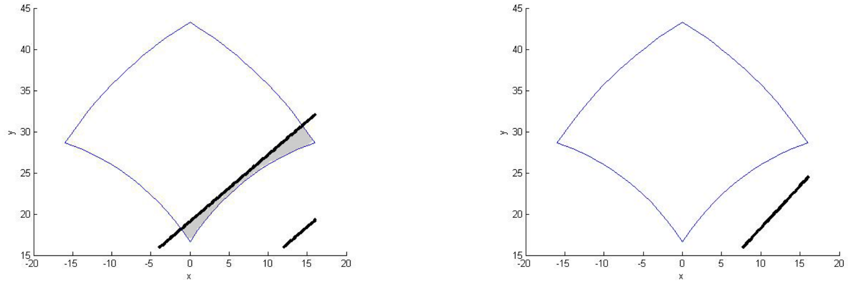

(g) $\theta = 80° \ F = 80N \ M = -1000N \cdot mm$

(h) $\theta = 80° \ F = 80N \ M = -200N \cdot mm$

Figure 3.6: Stable area overlap with the workspace

the location of the platform CG must satisfy the following inequalities

$$\begin{aligned} (x+a)^2 + y^2 &< L^2 \\ (x+a)^2 + y^2 &> l^2 \\ (x-a)^2 + y^2 &< L^2 \\ (x-a)^2 + y^2 &> l^2 \end{aligned} \tag{3.7}$$

$$1 - \frac{(2M + 2yF_x - 2xF_y - 2xG)^2}{D^2 (F_y + G)^2} > S_d \tag{3.8}$$

where S_d is the desired stability margin value, assuming a stability range of $S_d \leq S \leq 1$. Rewriting Eqn.(3.8) with the desired platform CG location on the left and the desired minimum stability margin level on the right gives

$$2yF_x - 2x\left(F_y + G\right) > -2M \pm D\left(F_y + G\right)\sqrt{1 - S_d} \tag{3.9}$$

Eqn.(3.9) represents the constraint of CG position for minimum stability requirement.

3.7 Geometrical and Physical Consideration

The FFSM represents the stability of the system without considering the geometrical and physical aspects of the robot. These aspects can be seen in the height, surface contact positions, and weight of the robot. Since these parameters directly affect the stability of the system, a modified FFSM (MFFSM) [29] is used to consider these parameters. The MFFSM is defined as

$$MFFSM = \overline{f} \cdot FFSM \cdot \left\{ \min \left[\frac{(p_i)^j}{h_i} \right] \right\} \tag{3.10}$$

where j=1 if the projection of the CG is inside or on the support polygon and j=-1 if it is outside of the support polygon, p_i represents the absolute distance from CG

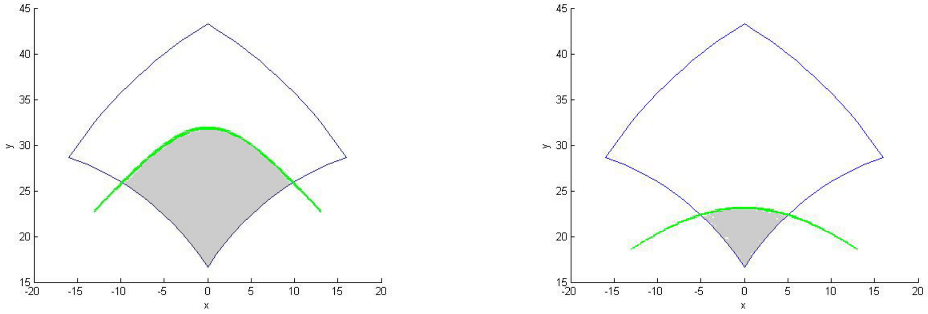

(a) $\theta = 0^\circ\ F = 30N\ M = 0N \cdot mm$ (b) $\theta = 0^\circ\ F = 33N\ M = 200N \cdot mm$

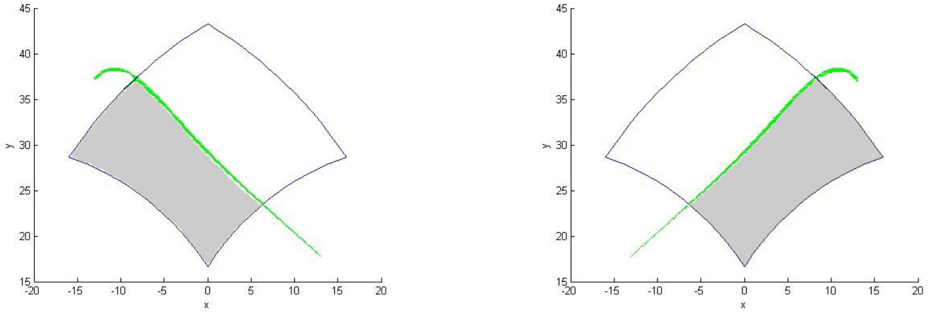

(c) $\theta = 10^\circ\ F = 30N\ M = 0N \cdot mm$ (d) $\theta = -10^\circ\ F = 30N\ M = 0N \cdot mm$

Figure 3.7: The stable workspace using MFFSM

to the corresponding foot contact point, h_i represents the absolute height of the CG with respect to the corresponding foot contact point, and $\overline{f}$ is the average foot force. The inclusion of $\left\{\min\left[\frac{(p_i)^j}{h_i}\right]\right\}$ allows for the determination of the tip over potential of the robot about the tip over points. When CG is outside of the support polygon, since $h_i < p_i$ and j=-1, the value of MFFSM will fall under minimum value for the posture robot can stand. By integrating Eqns. (3.6) and (3.10), the stability equation is given as

$$S = \frac{(p_i)^j}{h_i} \cdot \overline{f} \left(1 - \frac{(2M + 2yF_x - 2xF_y - 2xG)^2}{D^2 (F_y + G)^2} \right) \tag{3.11}$$

Figure 3.7 shows a few example stable workspace configurations given different loading conditions with a MFFSM value equivalent to FFSM=0.6. The loading conditions varied the magnitude and direction of the external force with M=0N, G=50N, and D=26cm. Compared to the linear stability margin boundaries of the FFSM, the stability margin boundaries using the MFFSM are defined by curves. In Figure 3.7, the grey area represents the stable workspace. Figure 3.7(a) and 3.7(b) indicate that an increment in the external force sharply affects the stability of the platform. Figure 3.7(c) and 3.7(d) shows the effect of changing the force direction. Similar to using the FFSM, changing the force angle causes the stability margin curves to transform based on a rotation. Integrating the MFFSM with the workspace makes the model more sensitive to height, force and force angle changes. From Figure 3.7(a) to 3.7(b), the force increases only by 3N. In Figure 3.7(c) and 3.7(d), the angle changes by ±10°. Compared to Figure 3.5, the sensitivity when using MFFSM is greater compared to using FFSM.

When using the FFSM as the stability criterion, the model assumed that the platform CG was always located in between the contact points. However, when using the MFFSM, the location of the platform CG relative to the contact locations is considered allowing the stable workspace algorithm to be applicable to robots with more complex structures, or in an environment with higher sensitivity requirement.

3.8 Analytical Stable Workspace Boundary Example

Validation of the stable workspace is completed using a simulated example. The parameters and loading conditions of the platform are $S = 0.9$, $G = 50$ N, $M = 0$, F_y = -10 N, $F_x = -10\sqrt{3}$ N, and $D = 50$ mm. The desired stability margin range is 0.9 to 1. Figure 3.8 shows the overlap of the desired stability area and the workspace of the platform. The left and right boundaries of the stable area are defined by FFSM=0.9. The following calculation demonstrates the derivation of the analytical boundary of the stable workspace.

Rotating the original coordinate frame by an angle θ, which is the angle between the margin of FFSM=0.9 and original y-axis, rotates the FFSM margin line to be perpendicular to the new x-axis. The location of the points in the new coordinate system can be calculated using the transformation

$$\begin{bmatrix} x' \\ y' \end{bmatrix} = \begin{bmatrix} \cos\theta & \sin\theta \\ -\sin\theta & \cos\theta \end{bmatrix} \begin{bmatrix} x \\ y \end{bmatrix} = \begin{bmatrix} x\cos\theta - y\sin\theta \\ y\cos\theta + x\sin\theta \end{bmatrix} \tag{3.12}$$

Using Eqn.(3.12), the position of all crossover points, p_l and p_0 in Figure 3.8, are given by

$$p_l = \begin{bmatrix} x \\ y \end{bmatrix} = \begin{bmatrix} \frac{l^2-L^2}{4a} \\ \sqrt{L^2 - \left(\frac{l^2-L^2-4a^2}{4a}\right)^2} \end{bmatrix} \tag{3.13}$$

$$p_0 = \begin{bmatrix} x \\ y \end{bmatrix} = \begin{bmatrix} 0 \\ \sqrt{l^2 - a^2} \end{bmatrix} \tag{3.14}$$

There are three workspace boundary curves included in the stable workspace shown in Figure 3.8. The three workspace boundary curves are given by

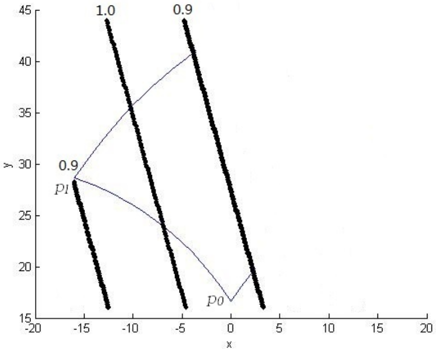

Figure 3.8: Stable workspace with FFSM=0.9

$$
\begin{aligned}
(x-a)^2 + y^2 &= L^2 \\
(x+a)^2 + y^2 &= l^2 \\
(x-a)^2 + y^2 &= l^2
\end{aligned}
\tag{3.15}
$$

where $a = 25$ mm, $L = 50$ mm, $l = 30$ mm. Rewriting the FFSM equation, the right hand side line with FFSM = 0.9 is given by

$$
y = \left(\frac{F_y + G}{F_x} \right) x + \frac{\sqrt{S} D \left(F_y + G \right) - 2M}{2F_x} \tag{3.16}
$$

Plugging in $S = 0.9$, $G = 50$ N, $M = 0$, $F_y =$ -10 N, $F_x = -10\sqrt{3}$ N, and $D = 50$ mm gives

$$
y = -2.31x + 54.77 \tag{3.17}
$$

With the right hand side boundary and the workspace boundaries given by Eqn.(3.15), the complete analytical solution to the stable workspace is given.

3.9 Stable Workspace Criterion

One possible criterion to evaluate the performance of the stable workspace of a robot, a possible way is to measure the area of the stable workspace. The total area

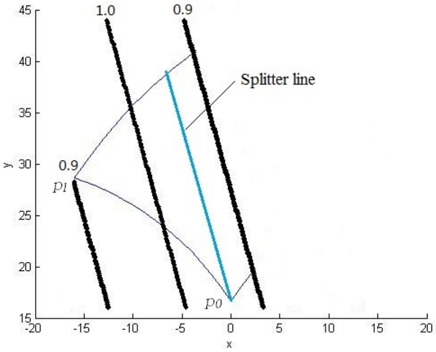

Figure 3.9: Bisecting the stable workspace for integration

of the stable workspace is obtained through integration. The total stable workspace area provides a metric to compare the stable workspace of different configurations and optimize parameter selection. To integrate over the stable workspace, a line bisecting the stable workspace is generated as shown in Figure 3.9. The bisection line starts at the bottom crossover point and runs parallel to the stability margin line. The stable workspace area is then given by

$$SW = \int_{x_0'}^{x_1'} \int_{(lower\ \ boundary)}^{(upper\ \ boundary)} dxdy \tag{3.18}$$

where x_1' is the position of abscissa of right boundary, which is perpendicular to new x-axis (also the x'-axis), and x_0' is the position of abscissa of left boundary (p_l' for this example). Assuming y=0 in the FFSM equation with FFSM=0.9, the value of x_1' can be found. The stable workspace area can then be found using

$$SW = \int_{p_l'}^{p_0'} dx' \int_{\sqrt{l^2-(x'+a)^2}}^{\sqrt{l^2-(x'-a)^2}} dy' + \int_{p_0'}^{x_1'} dx' \int_{\sqrt{l^2-(x'-a)^2}}^{\sqrt{L^2-(x'-a)^2}} dy' \tag{3.19}$$

All relations between (x', y') and (x, y), p_0', p_l' and p_0, p_l, follow the transformation given by Eqn.(3.12). The stable workspace area can then be found by substituting all related parameters.

Chapter 4

Simulation and Experimental Results

4.1 Stable Workspace of a Scalable Hexapod Robot

This section demonstrates the advantages of scalability on the stable workspace. The scalable hexapod robot is executing a horizontal machining process. The basic hardware configuration is as shown in Figure 4.1. A scalable hexapod robot will have a maximum and minimum configuration. The leg length in the minimized configuration is $l = 80$ mm. The length in the maximized configuration is $L = 150$ mm. The variation of leg length from minimized to maximized configuration is $\Delta = 70mm$. The machining path is constant and horizontal. Figure 4.2 shows the stability of the robot while machining given $G = 50$ N, $F = 30$ N, and $\theta = 20°$. The height change between two configuration is $\Delta h \approx 80\ mm$. The criterion of stability uses FFSM.

During the machining process, the robot will have to change foot locations to cover the entire desired machining path. Each leg shift or walk covers a small section of the machining path with an entry and exit point. In Figure 4.2, each cycle represents the stability change of the robot as it moves from the entry point to the exit point

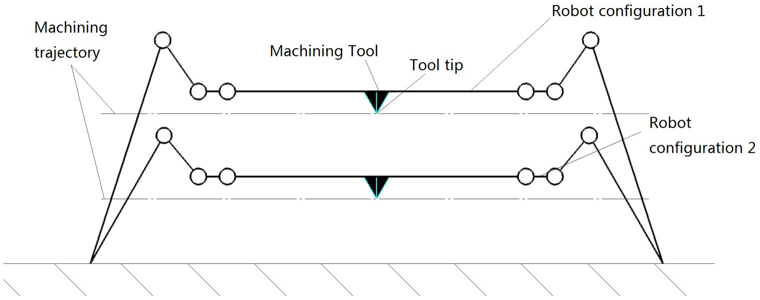

Figure 4.1: Example of a horizontal machining process

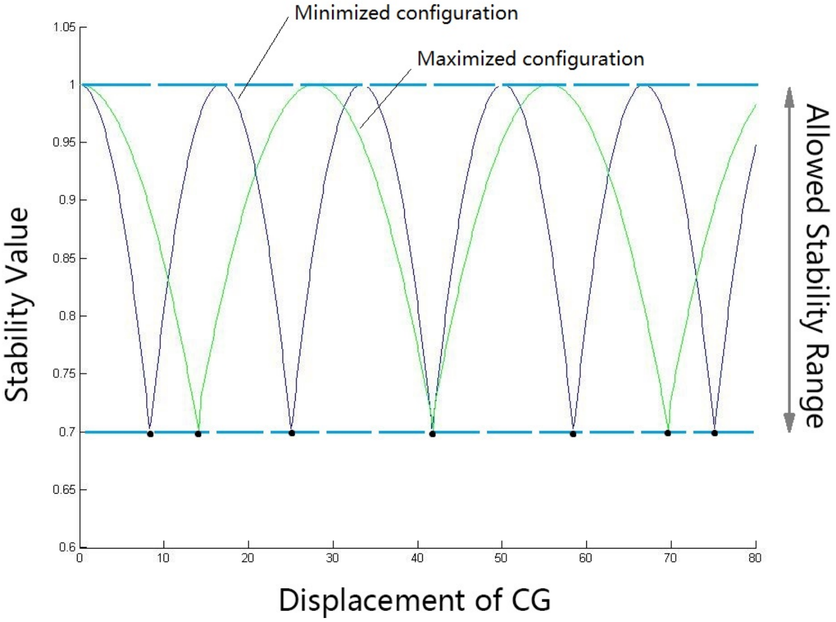

Figure 4.2: The stability of the robot during the simulated horizontal machining process

of the machining path it is currently traversing. Machining starts from the position with minimum value of stability (in this example it is set to 0.7), to the other lower limit, and then move to next position point by walking to reset its stability value. The bullet points on the lower allowed stability margin are the positions where feet of robot would change to the next configuration in a non-continuous manner through walking. In the period of time between the crest and trough of the wave, the robot is machining while in the stable workspace.

The blue curve represents the stability value change of robot with minimized con-

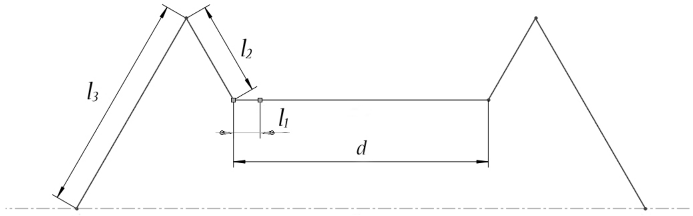

Segment Par.	Value
l_1	20mm
l_2	70mm
l_3	100mm
d	170mm

Figure 4.3: Dimension of traditional hexapod robot

figuration when doing machining. The green curve represents the maximized configuration. Comparing the plots, the stability changes slower after the robot transforms from minimized size to maximized at a certain position (without movement of feet). The amount of machining needs less steps. This means the robot can complete more work at a certain location, due to a scaled workspace. The stable workspace is enlarged along with workspace. It is flexible to set either configuration as default to keep the original features and gain extra functions, such like large workspace, better mobility, ride through capability and so on.

The size of robot design in later sections is chosen to be similar to a traditional

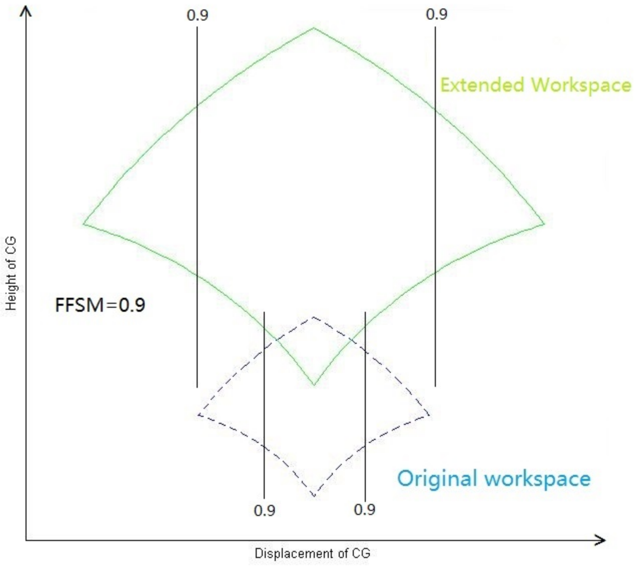

Figure 4.4: Workspace and stability comparison

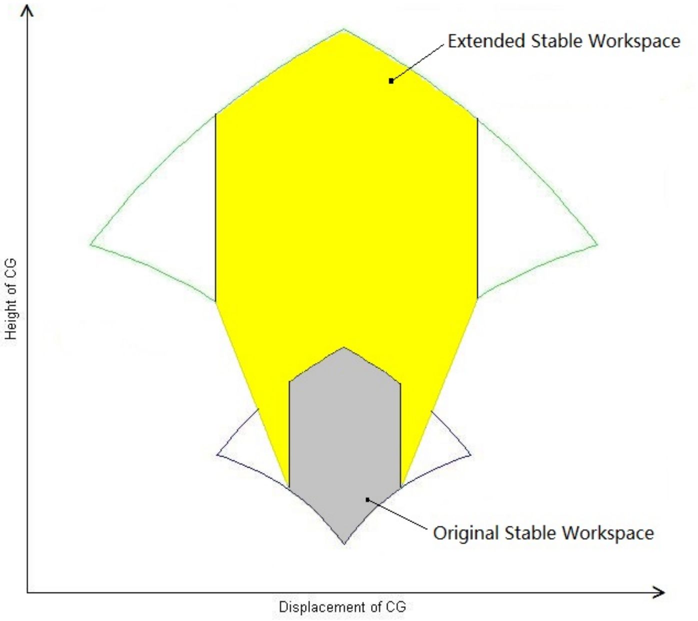

Figure 4.5: Conversion of stable workspace

hexapod robot [4] which is mentioned in Chapter 1. This is to realize the scalability on original model. Figure 4.3 gives several main parameters of robot dimension. The 2 lengths have part of extension after leg transformation. The dimensions for the lengths l_1, l_2 and l_3 are taken to be simplified to make equivalent model. So that in the model $l = 50$ mm and $L = 170$ mm. The variation of leg length with scalable design from minimized to maximized configuration is $\Delta = 120\ mm$.

Figure 4.4 compares the original workspace and stability between the original configuration of robot and the one with extended leg. As the figure shows, the area enclosed with dash lines is the original/minimized workspace area, and the one enclosed with solid lines is the extended/maximized area. The size of extended workspace is about triple the original one. Since the height of robot rises, the lowest point which CG could reach also rises.

There are also stability margins (black lines) shown in Figure 4.4 with FFSM=0.9 (0.9 is an example value) and no external factors applied on it. It can be observed in the figure that the stable workspace area also extends with the same scale of workspace.

With the variable length of leg, the stable workspace is enhanced, as shown in Figure 4.5. The grey area is the original stable workspace. The yellow area is the extended stable workspace. Thus, with the convertible stable workspace, the robot can reach variable requirements of tasks, with the balance between stable workspace size and robot size.

4.2 Robot Stability Demonstration

The goal of experiment is to simulate machining on a part with a curved profile where the tool center point of the robot attached to the platform has to be perpendicular to the curve at each point. This simulated machining will realize one cycle of machining as the simulation shown in Figure 4.2. The lateral distance of platform motion is 25mm and the maximum height difference during machining is 30mm. The robot works following a curve as shown in Figure 4.6. As the same process described in previous section, the path is given within Arduino Pilot. It is translated into command of angles for motors and distributed to leg boards.

During the experiment process, the foot contact points on the ground do not change. The platform keeps its direction as the tangential direction of machining

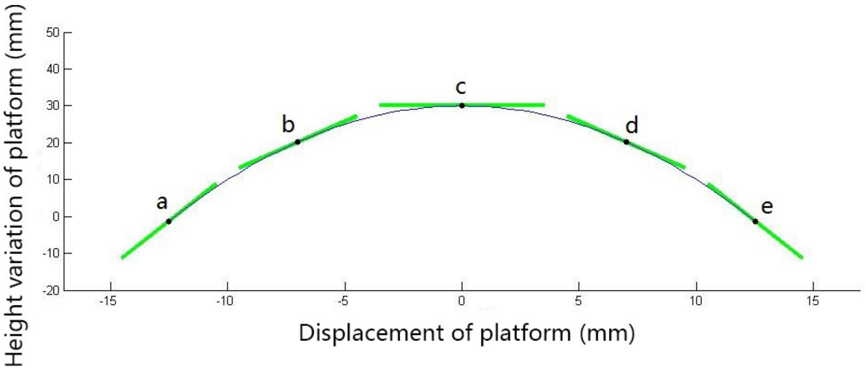

Figure 4.6: Simulation of machining curve

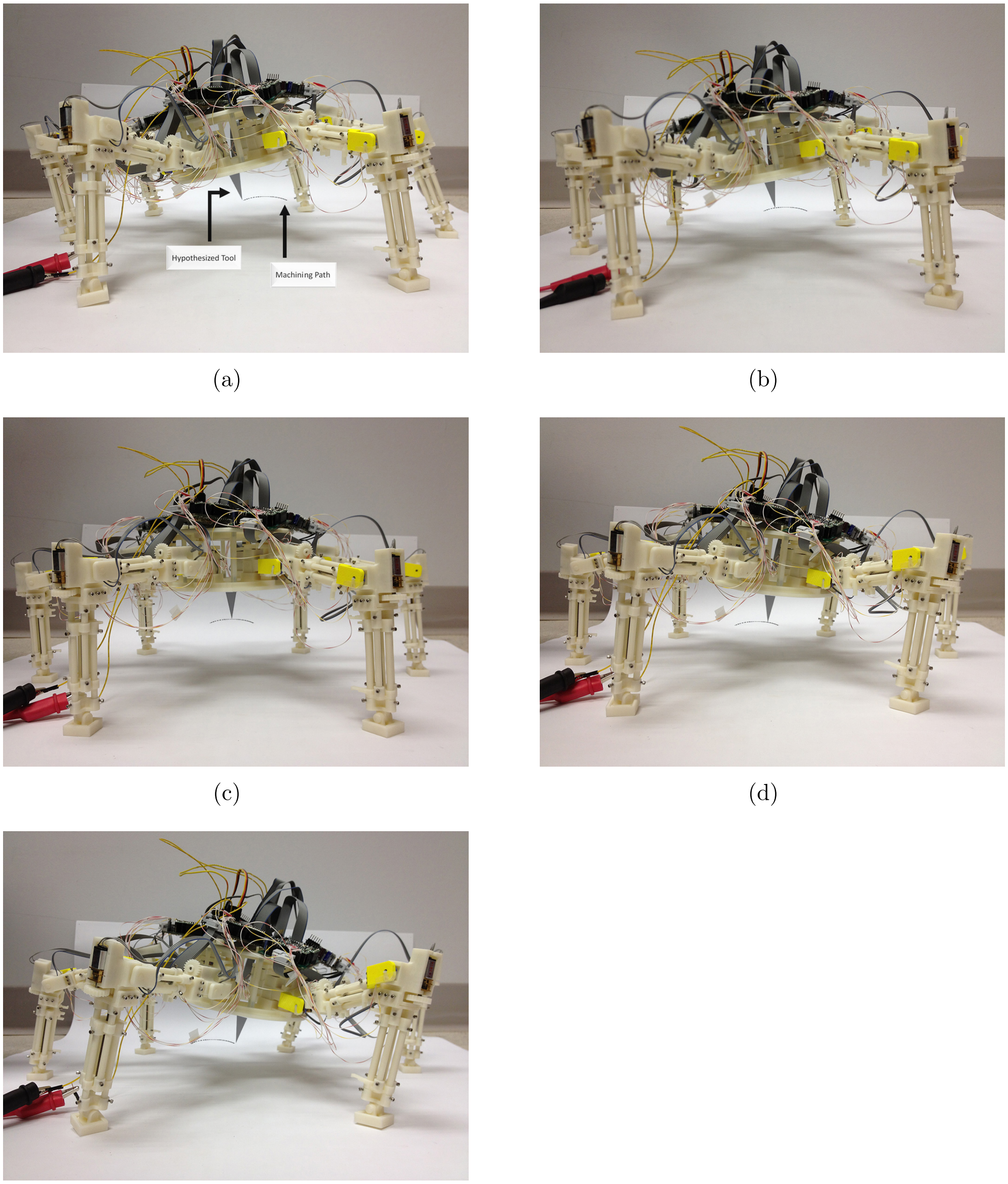

(a)

(b)

(c)

(d)

(e)

Figure 4.7: Machining experiment

path, which means the tool would be always perpendicular to the part surface. In Figure 4.7, the grey triangle under the robot body represents a hypothetical machining tool connecting to the robot. The dash line represents the machining path, which is the same as Figure 4.6. Each figure of Figure 4.7 has its corresponding position status point in Figure 4.6, with the same sequence number.The tip of tool is on the path. The platform starts from left, as shown in Figure 4.7(a), where the platform is farthest away from horizontal. The platform keeps moving as shown in Figure 4.7(b), with the intersection angle between platform and horizontal decreasing. The robot reaches the highest point in the middle of the curve, as shown in Figure 4.7(c), where the platform comes to be horizontal. The height is also at the highest level at this point. After the highest point, the height comes down. The orientation of platform changes to be opposite to the process from Figure 4.7(a) to 4.7(c), as shown in Figure 4.7(d). The platform reaches the lowest point on right as shown in Figure 4.7(e), where the platform turns to be farthest away from horizontal again. It stops working after it reaches the other lowest point. By this process, the robot does a simulation of orientation changing when doing machining.

4.3 Robot Scalability Demonstration

The goal of this experiment is to validate that using the scalability of the robot can traverse a wide gap, which regular size robot cannot. The width of gap is 140mm. This width is selected because robot cannot step over the gap with this width with its collapsed configuration.

Figure 4.8 shows a comparison between contracted and extended status of the robot. From the view of Figure 4.8(a) to 4.8(b), the robot obviously becomes higher and covers larger area. All legs are fully extended. The length of upper leg is extended from 96mm to 126mm, and the lower leg is from 112mm to 157mm.

Figure 4.9 gives an example of typical application of the scalable robot. The ability of robot for crossing a gap may be insufficient when meets a wide gap with its original size. In the left part of figure, the leg of robot with original length could

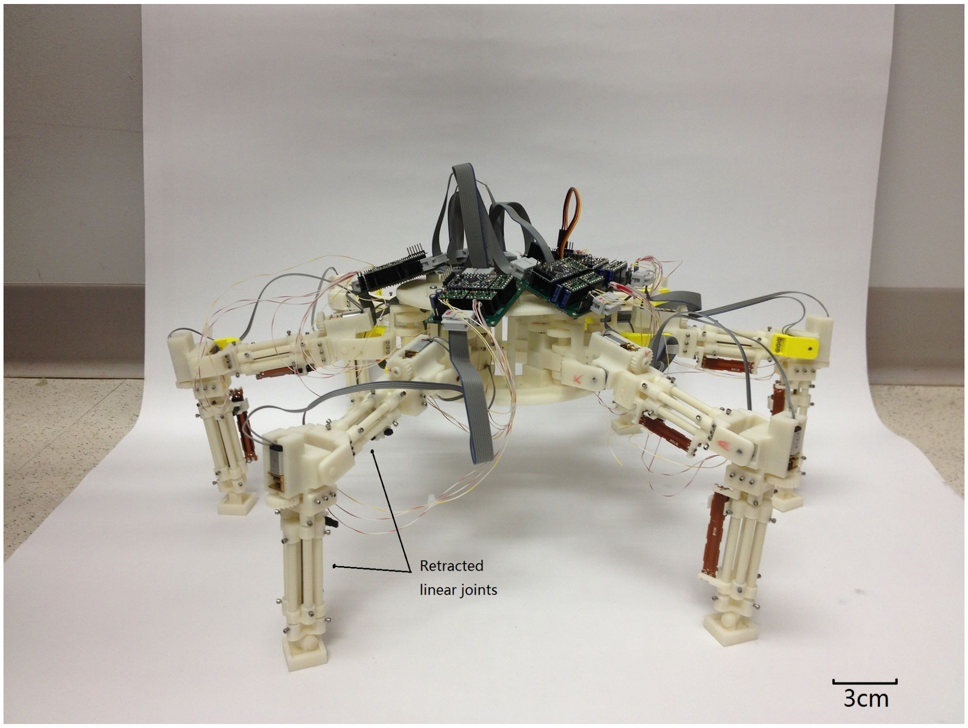

(a) Collapsed form

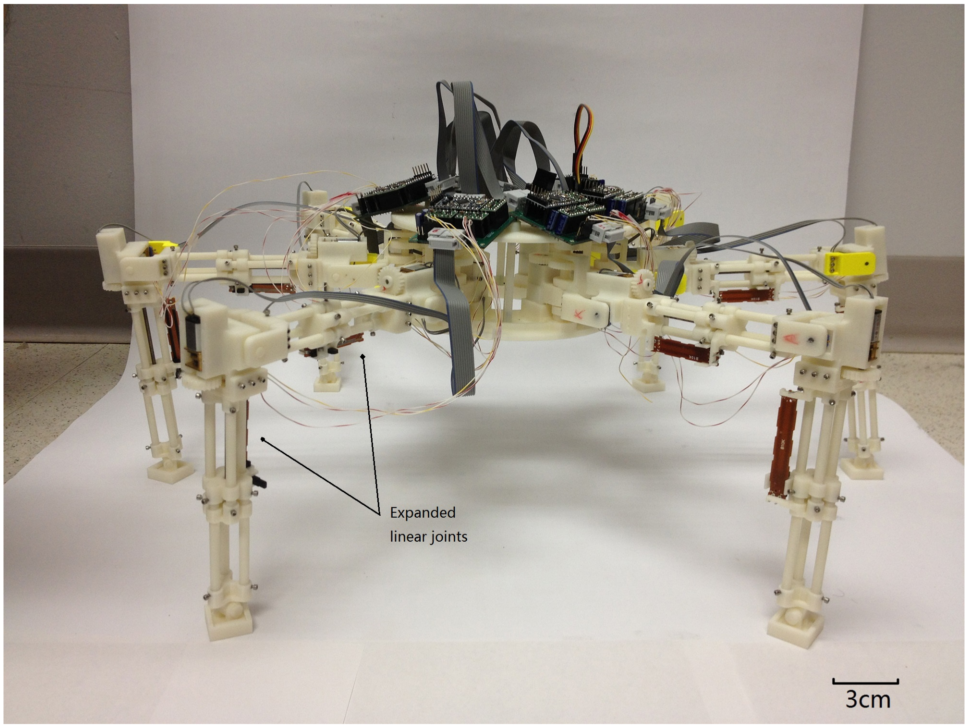

(b) Expanded form

Figure 4.8: Scalable status comparison

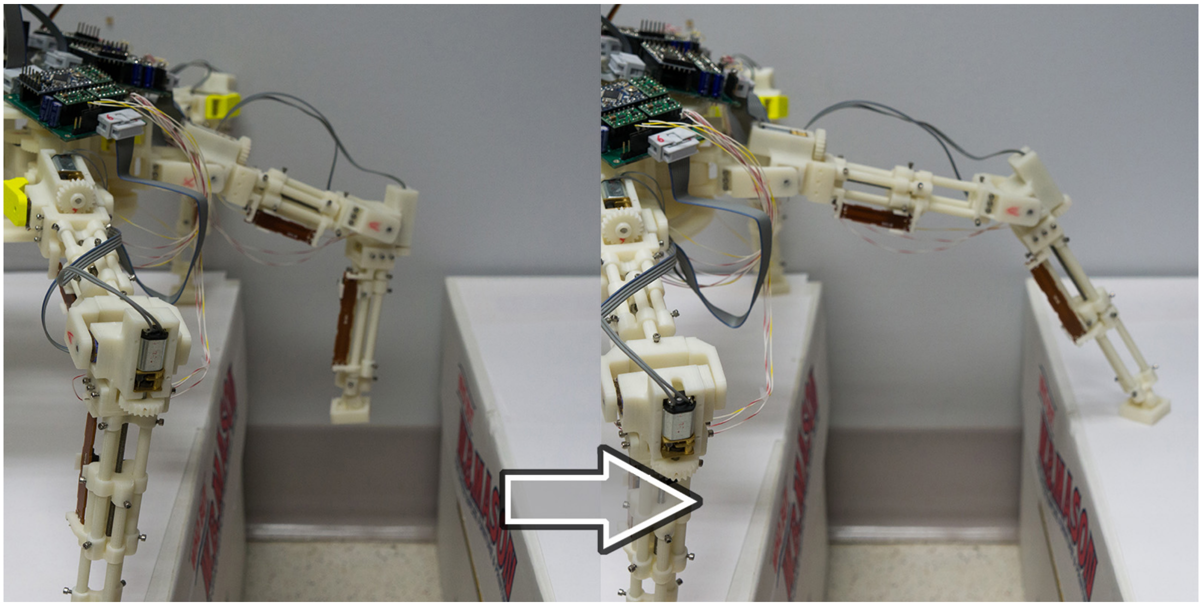

Figure 4.9: Application example for function of leg extension

not reach the other side of gap. After leg is extended, as shown in the right part of figure, the foot could contact the other side of gap, or even has some allowance.

Through the process of stepping over the gap, the robot makes each posture separately. The position of each step is calculated with an inverse kinematic model embedded in the main controller with a given path as the input parameter. The separate destinations for robot movement is then inputted to controller with the sequence of steps, to make actions at each desired position.

From the start posture as shown in Figure 4.10(a), the leg which is nearest to the other side gap is fully extended and try to reach the other side. The 2 legs next to the first leg both on left and right is partial extended after the first leg is extended, to rise the body platform to change the working configuration of robot. Also, rising up the body platform can reduce the load on ankle joint when completing a step.

When the first leg reaches the other side of gap, the ankle joint runs to bring the robot body moving towards the other side. The next 2 leg come up with the first leg across the leg, as shown in Figure 4.10(b). When crossing, they keep extending until fully extended. At the moment that the center of gravity of robot reach the

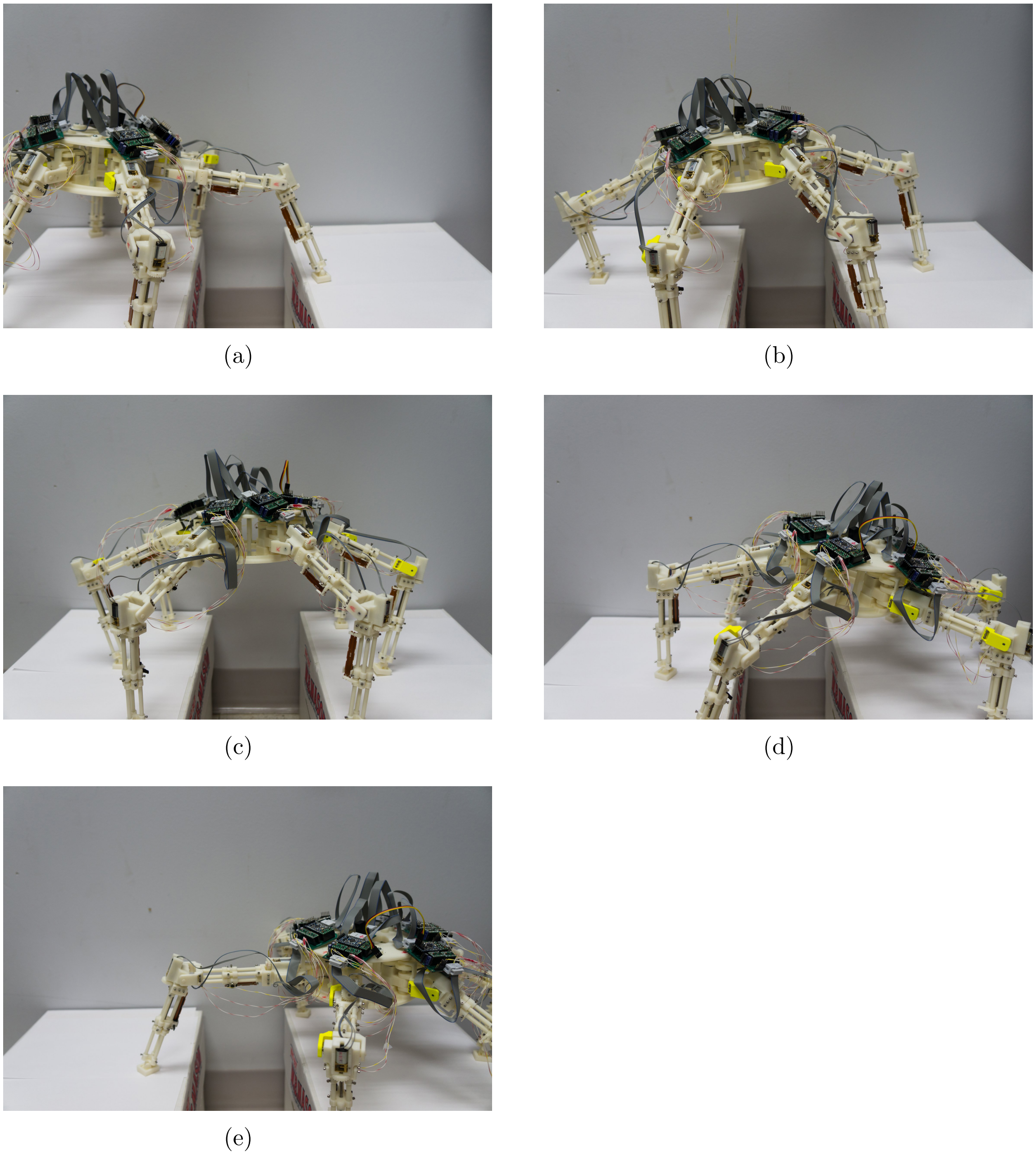
(a)

(b)

(c)

(d)

(e)

Figure 4.10: Gap traversing experiment

middle of gap, the legs are all fully extended, as shown in Figure 4.10(c). With this configuration, the ability of crossing obstacles reaches the highest level.

After the middle period, the ankle joints of the first 3 legs keeps running to bring the robot body. The first 3 legs begins to shorten its length, to bring the robot body further to the direction of travel, as shown in Figure 4.10(d). The next 2 legs after the first 3 legs will come up to the other side then as shown in Figure 4.10(e) and begins to shorten their length too, to restore the regular configuration before encountering the gap. The rest one leg will follow the body to be transferred across.

The process from Figure 4.10(c) to 4.10(e) is opposite mirror of the one from Figure 4.10(a) to 4.10(c). With such example process, the robot would have ability to cross some irregular terrain which with regular size robot could not.

Chapter 5

Discussion and Future Work

From the demonstration through experiment, the goal of design has been reached. The robot with the scalable structure has a flexible stable works, which enhances the workspace of the robot with a rigid structure. The workspace enlarges approximate triple as original configuration with the designed scalability. From what was performed, the robot is demonstrated to be able to handle the tasks with variable sizes requirement.

However, there are still some drawbacks open to discussion. The following is a list of notes which is recorded during a series design process and experiment. Such specifications but not limited are needed to be improved in future version.

Better materials

The current version is for prototype, so it is made with plastic by 3D-printer. Plastic parts are easy to be designed and manufactured with complex structure. But they are always with abrasive wear. Parts need to be replaced after a period of work, especially for some parts connecting to structure with quite frequent action. For example, the part connecting to motor and the next part of leg is often abraded which is caused by a large torque of motor. With a considerable weight of leg with many devices, plastic is sometimes soft to be impacted by gravity of leg and torque. The D-shape port set on the shaft of motor is usually worn to be a hole. The future design is desired to use metal, such like aluminum with enough strength and light weight.

More standard connection

The current design used a lot of non-reusable and fabricable connection which is not convenient to be replaced with spare parts. Non-reusable connection is such like the linkage using glue, since the glue is not able to be split once dry. If it is needed to be replaced for some reason, the parts on both sides would be broken. Fabricable connection is for example, most bolts screws into the terminal parts reaching the end of bolt. There is no special screw thread on both parts. Thus when the bolt is passing, it is under a press fit and produces heat, which may change the shape of plastic around. This works for first time connection, but in future screwing in and out the connection would be loose.

Besides, the housing for sensors, motors and controllers don't fit their shape perfectly. This also make the whole assembly unfirm. The connection to sensor also lacks of standard connection. Most connection is made by soldering, which is weak under fold caused by motion of robot. It is also hard to be fixed once broken unless disassemble related parts and re-solder the wire and port. A good example is the power supplement from motor drivers to motor. The header is a standard connection part, which could be repeated used with no abrasion.

Therefore, firm and reusable connection with standard parts is needed. Standard parts like bolts with nuts on both parts side, slot with flexible hook, addition lock parts and so on.

Less number of parts for better assembling feasibility

The current design has about 200 parts in total. This case is caused by the design process. When doing the design, the consideration is more on the function realization but less on integration and standard of mechanism. Thus the whole structure is a simple stack of functional parts, with less mutual arrangement and support among parts. For instance, the amount of guide rails is 6 per prismatic joint. So there are more than 70 parts in total only for the prismatic joint. If this structure is changed with a group of sleeve, the amount of parts will be reduced to 30% of original. For the whole robot, the amount of parts is hopeful to cut down to 50 according to estimates.

Fabrication Tolerance

The current manufacturing way is Dimension SST 1200ES Rapid Prototype Machine. This machine is with a manufacturing error of 0.15mm. This cannot be ignored special at some position of insertion and sliding pair. A lot of hand work of polishing is made on raw parts. Future version may request the manufacture has better machining precision, since materials of metal is hard to be fixed on size error.

Integrated Control Board

The initial board design is an integrated board, but it lacks the characteristic of modularity. Thus the modules could not be replaced or updated separately. The later board design realize the modularization, but it makes it hard to arrange the board compactly for the data and power wires connecting the boards. Future design would regain the task to make the board return to an integrated view. If possible, the design may break the sub-controllers and motor drivers into more raw parts of processors, capacitors and resisters. To place them breaking the boundary of original PCB can make the control reach a more compact size, though it increase the amount of work that soldering the parts onto board. Some automatic manufacture method may be useful.

More Reliable Traces Design

The current design of control board has realize all desired function, but it is not robust enough for regular use. There are some specifications should be improved which is found during experiment.

It should be designed with more electrical isolation. The current traces connect the parts directly with seldom devices to prevent some accidental cases, like reverse current and impulse wave. This may also affect the stability of the circuit. If the logic circuit power supplement is affect by some strong current parts, it may get happened power lost and reset. Another example is, the communication to computer cannot coexist with on board power supplement. The 5V power of USB port may cause reverse current back to DC voltage convertor, which may damage the convertor in a short time. This make it hard to monitor some real time data when processing experimental motion.

Some testing point should be setup on board. It is not convenient to test if the circuit is unobstructed when the board is working. Now it can only attach the opposite side contact point of pins, which needs to move the board from robot top. If the test point around some crucial devices on board is setup, it would be more convenient to monitor the work status of separate of board.

Future design may also need some additional power and data socket, to satisfy the requirement of some other external devices. This may make the system has better expansibility. It can add such as IMUs, additional senors and so on for upgrade.

Chapter 6

Conclusion

This research designed and fabricated a new scalable hexapod robot as a mobile machining platform and developed a lateral stable workspace criterion for real-time monitoring and control of the robot. The scalable hexapod robot aims to replace humans from having to work in constrictive and hazardous environments during the regular maintanance and inspection of today's societal structures.

The new scalable hexapod robot design enhances the workspace of traditional hexapod robots by incorporating two additional prismatic joints into each leg of the system. The robot was fabricated using a rapid prototype machine and assembled in-house. A distributed control architecture was utilized in which each leg had a dedicated controller to handle the leg position. Use of a distributed control architecture allows the main controller to focus on the stability and workspace calculations. All of the electronic printed circuit boards were designed and assembled in-house. Two iterations of the electronics were completed.

To validate the control architecture and demonstrate the advantages of a scalable design, two physical experiments were performed. The first physical experiment demonstrated the ability for the scalable hexapod robot to orient itself to multiple points along a machining path. The second physical experiment demonstrated the ability for the robot to cross a wide gap using the scalability of the system.

To maintain stability and workspace while machining, a stable workspace criterion was developed based on the Foot Force Stability Margin. The stable workspace criterion can be used in design optimization of the hexapod robot or in real-time control and monitoring of the system. The lateral workspace and stability of the scalable hexapod was analyzed under different external loading conditions. The effects of stability on the lateral workspace was determined and an analytical solution to the boundary of the lateral stable workspace was presented. The geometrical and physical effects of the robot on the stable workspace were determined by utilizing the Modified Force Based Stability Margin. Simulation results were presented that demonstrates the stable workspace advantages of incorporating scalability into the robot design.

Appendix A

Schematics and Layout of Electronics

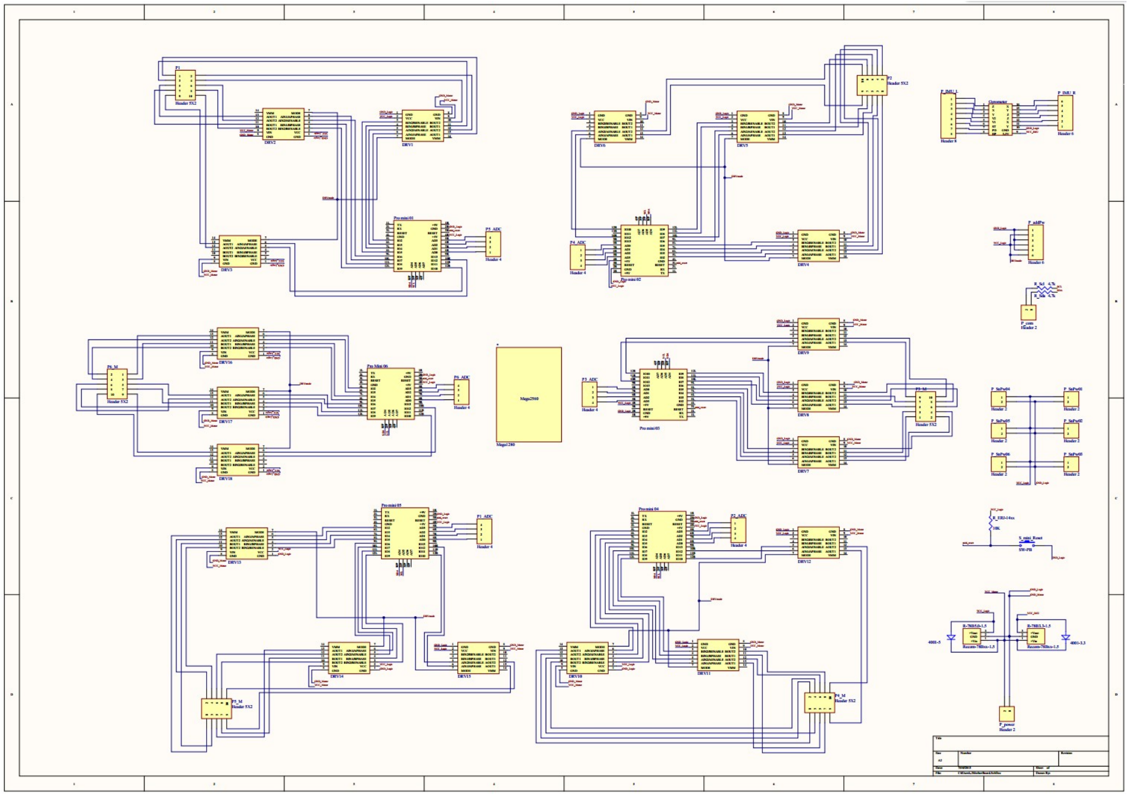

Figure A.1: An overview of first generation control board schematic

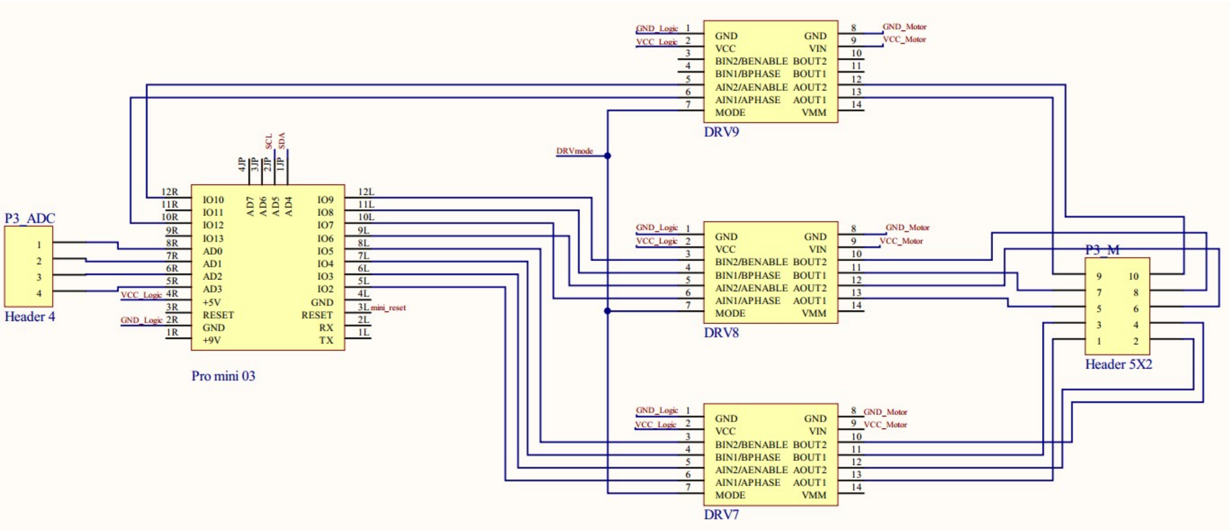

Figure A.2: Schematic of sub-controller and motor module

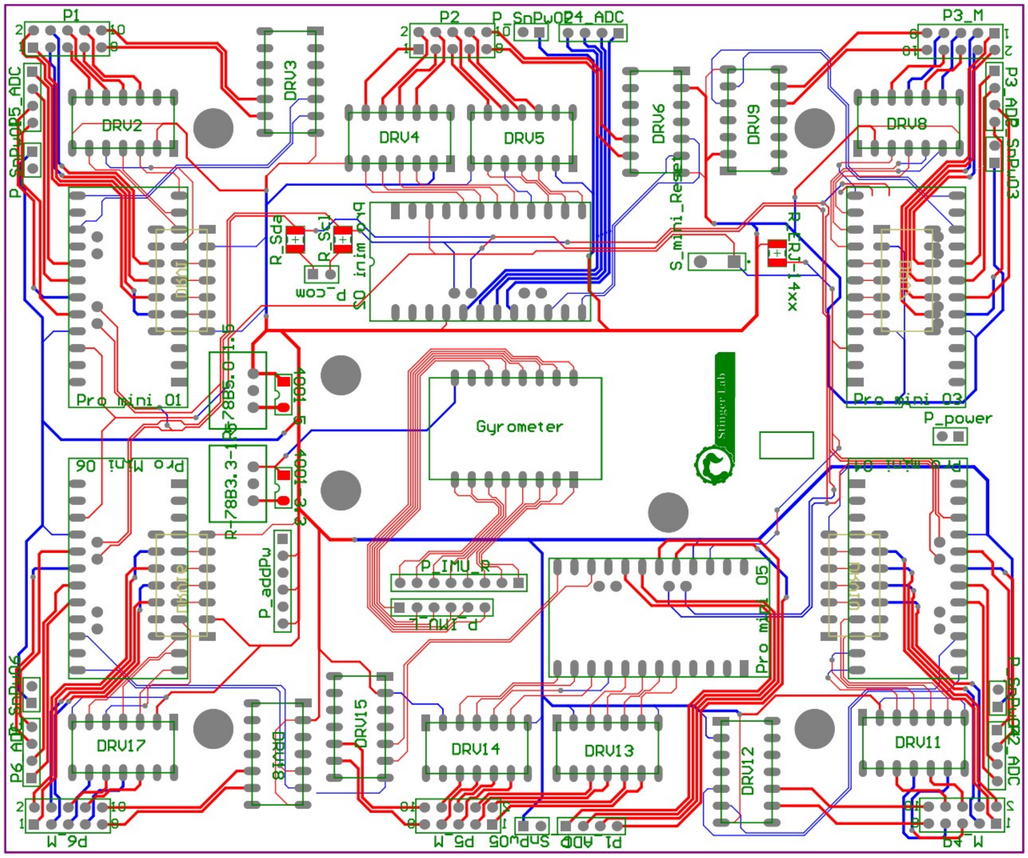

Figure A.3: PCB layout of first generation board

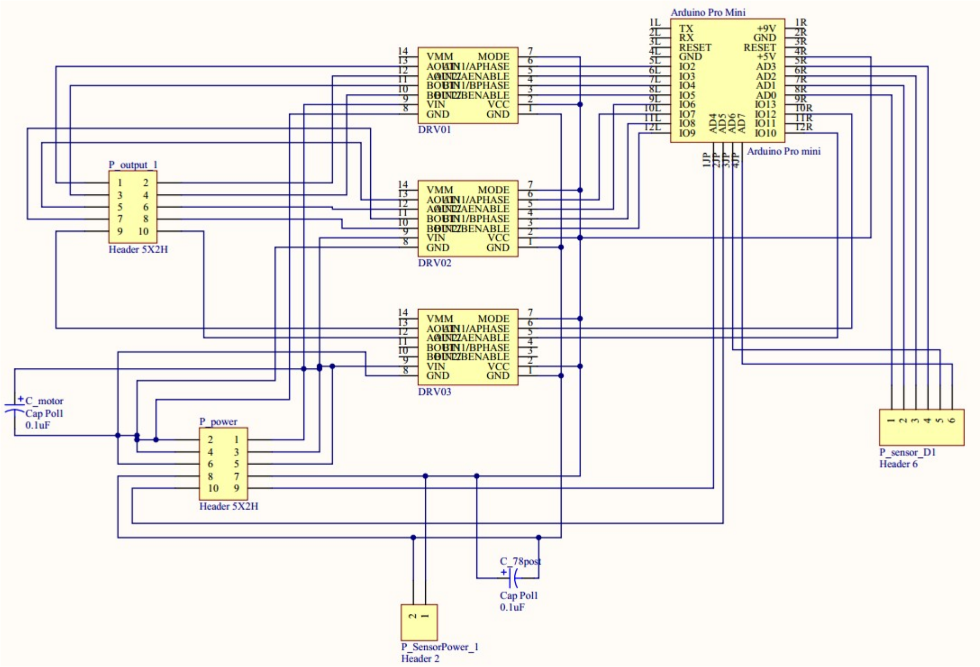

Figure A.4: Schematic of second generation leg board

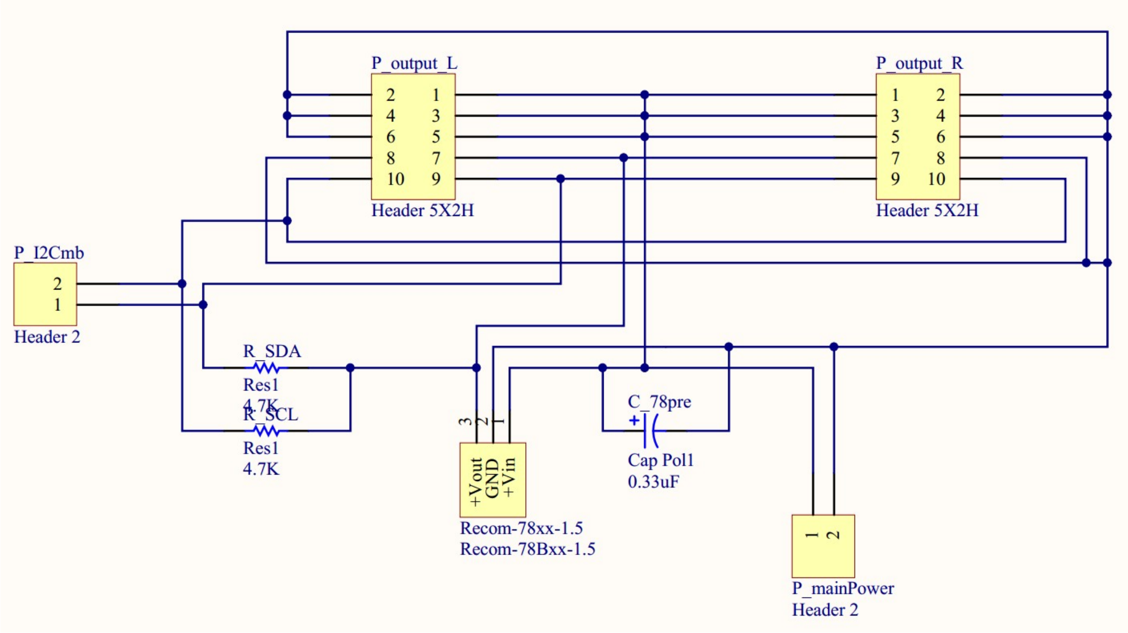

Figure A.5: Schematic of second generation power board

Appendix B

Embedded DC Motor Control Program

```
//This program contains the process of reset to home position and move to one more destination
#include <Wire.h>//declare the library of I2C
#include <Servo.h>
//set feedback pins input
const int hippospin=A2;
const int kneepospin=A1;
const int anklepospin=A0;
int hipposval,kneeposval,ankleposval;
int hippostarg,kneepostarg,anklepostarg;
//set home position value
const int hipposhome=530;
const int kneeposhome=0;
const int ankleposhome=180;
//initiate communication parameters int i;byte x=0;

void setup()      //Initialization
{ Serial.begin(9600);
Wire.begin(1); // join i2c bus and set slave number
for(i=2;i<=12;i++) //initialize the mode of output pins
pinMode(i, OUTPUT);
//initiate home position
//give original target as home position
hippostarg=hipposhome;
kneepostarg=kneeposhome;
anklepostarg=ankleposhome;
//————Reset to home pos—————
hipposval=analogRead(hippospin);
kneeposval=analogRead(kneepospin);
ankleposval=analogRead(anklepospin);

//KNEE
if(kneeposval<512)
{ while(abs(kneeposval-kneeposhome)>15)
{ digitalWrite(7, LOW);
analogWrite(6, 150);
kneeposval=analogRead(kneepospin);}
digitalWrite(7, LOW);
analogWrite(6, 00);}
if(kneeposval>512)
{ while(abs(kneeposval-kneeposhome)>15)
{ digitalWrite(7, HIGH);
analogWrite(6, 150);
kneeposval=analogRead(kneepospin);}
digitalWrite(7, LOW);
analogWrite(6, 00);}
if(abs(kneeposval-kneeposhome)<15)
{ digitalWrite(7, LOW);
analogWrite(6, 00);
kneeposval=analogRead(kneepospin);
delay(50);}
```

```
//ANKLE
if(ankleposhome<ankleposval && ankleposval<=692)
{ while(abs(ankleposval-ankleposhome)>15)
{ digitalWrite(2, LOW);
analogWrite(3, 150);
ankleposval=analogRead(anklepospin);}
digitalWrite(2, LOW);
analogWrite(3, 00);}
if(ankleposhome>ankleposval || ankleposval>692)
{ while(abs(ankleposval-ankleposhome)>15)
{ digitalWrite(2, HIGH);
analogWrite(3, 150);
ankleposval=analogRead(anklepospin);}
digitalWrite(2, LOW);
analogWrite(3, 00);}
if(abs(ankleposval-ankleposhome)<15)
{ digitalWrite(2, LOW);
analogWrite(3, 00);
ankleposval=analogRead(anklepospin);
delay(50);}

//HIP
if(hipposhome>hipposval)
{ while(abs(hipposval-hipposhome)>15)
{ digitalWrite(12, HIGH);
analogWrite(10, 150);
hipposval=analogRead(hippospin);}
digitalWrite(12, LOW);
analogWrite(10, 00);}
if(hipposhome<hipposval)
{ while(abs(hipposval-hipposhome)>15)
{ digitalWrite(12, LOW);
analogWrite(10, 150);
hipposval=analogRead(hippospin);}
digitalWrite(12, LOW);
analogWrite(10, 00);}
if(abs(hipposval-hipposhome)<15)
{ digitalWrite(12, LOW);
analogWrite(10, 00);
hipposval=analogRead(hippospin);
delay(50);}}
```

```
//main program
void loop()
{//motion based on parameters from master
hipposval=analogRead(hippospin);
kneeposval=analogRead(kneepospin);
ankleposval=analogRead(anklepospin);
anklepostarg=248
kneepostarg=0
hippostarg=543
//ANKLE
if(anklepostarg<ankleposval && ankleposval<=692)
{ while(abs(ankleposval-anklepostarg)>15)
{ digitalWrite(2, LOW);
analogWrite(3, 150);
ankleposval=analogRead(anklepospin);}
digitalWrite(2, LOW);
analogWrite(3, 00);}
if(anklepostarg>ankleposval || ankleposval>692)
{ while(abs(ankleposval-anklepostarg)>15)
{ digitalWrite(2, HIGH);
analogWrite(3, 150);
ankleposval=analogRead(anklepospin);}
digitalWrite(2, LOW);
analogWrite(3, 00);}
if(abs(ankleposval-anklepostarg)<15)
{ digitalWrite(2, LOW);
analogWrite(3, 00);
ankleposval=analogRead(anklepospin);
delay(50);}

//KNEE
if(kneeposval<512)
{ while(abs(kneeposval-kneepostarg)>15)
{ digitalWrite(7, LOW);
analogWrite(6, 150);
kneeposval=analogRead(kneepospin);}
digitalWrite(7, LOW);
analogWrite(6, 00);}
if(kneeposval>512)
{ while(abs(kneeposval-kneepostarg)>15)
```

```
{ digitalWrite(7, HIGH);
analogWrite(6, 150);
kneeposval=analogRead(kneepospin);
}
digitalWrite(7, LOW);
analogWrite(6, 00);}
if(abs(kneeposval-kneepostarg)<15)
{ digitalWrite(7, LOW);
analogWrite(6, 00);
kneeposval=analogRead(kneepospin);
delay(50);}

//HIP
if(hippostarg>hipposval)
{ while(abs(hipposval-hippostarg)>15)
{ digitalWrite(12, HIGH);
analogWrite(10, 150);
hipposval=analogRead(hippospin);}
digitalWrite(12, LOW);
analogWrite(10, 00);}
if(hippostarg<hipposval)
{ while(abs(hipposval-hippostarg)>15)
{ digitalWrite(12, LOW);
analogWrite(10, 150);
hipposval=analogRead(hippospin);}
digitalWrite(12, LOW);
analogWrite(10, 00);}
if(abs(hipposval-hippostarg)<15)
{ digitalWrite(12, LOW);
analogWrite(10, 00);
hipposval=analogRead(hippospin);
delay(50);}}

//run this when recieve letters from master
void receiveEvent(int howmany)
{ // loop execute, until the last letter of data packet
while( Wire.available()>1)
{ anklepostarg=Wire.read();}
while( Wire.available()>1)
{ kneepostarg=Wire.read();}
while( Wire.available()>1)
{ hippostarg = Wire.read();}}
```

References

[1] A. Iborra, B. Alvarez, F. Ortiz, F. Marin, C. Fernandez, and J. Fernandez-Merono, “Service robot for hull-blasting,” in *Industrial Electronics Society, 2001. IECON ’01. The 27th Annual Conference of the IEEE*, vol. 3, 2001, pp. 2178–2183 vol.3.

[2] J.-K. Oh, A.-Y. Lee, S. M. Oh, Y. Choi, B.-J. Yi, and H. won Yang, “Design and control of bridge inspection robot system,” in *Mechatronics and Automation, 2007. ICMA 2007. International Conference on*, 2007, pp. 3634–3639.

[3] L. Qu, M. Agheli, and S. Nestinger, “Lateral stable workspace of hexapod walking machines with constant orientation platform,” in *Mechatronics and Embedded Systems and Applications (MESA), 2013 IEEE/ASME International Conference on*, 2013.

[4] “Lynxmotion bh3-r hexapod robot kit - bh3rca-blk-645.” [Online]. Available: http://www.robotshop.com/lynxmotion-bh3-r-hexapod-robot-kit-blk-645a.html

[5] S. Fujii, K. Inoue, T. takubo, and T. Arai, “Climbing up onto steps for limb mechanism robot asterisk,” in *23rd International Symposium on Automation and Robotics in Construction*, 2006, pp. 225–230.

[6] C. Choi, B. Park, and S. Jung, “The design and analysis of a feeder pipe inspection robot with an automatic pipe tracking system,” *Mechatronics, IEEE/ASME Transactions on*, vol. 15, no. 5, pp. 736–745, 2010.

[7] “3d cad design software solidworks.” [Online]. Available: http://www.solidworks.com/

[8] “298:1 micro metal gearmotor hp.” [Online]. Available: http://www.lynxmotion.com/p-395-ssc-32-servo-controller.aspx

[9] “Sv01a103aea01r00 murata electronics north america.” [Online]. Available: http://www.digikey.com/product-detail/en/SV01A103AEA01R00/490-7023-2-ND/2604831

[10] “Force sensitive resistor 0.5.” [Online]. Available: https://www.sparkfun.com/products/9375

[11] "Ntm prop drive 35-36a 910." [Online]. Available: http://www.hobbyking.com/hobbyking/st-ore/__14847__NTM_Prop_Drive_Series_35_36A_910Kv_350W.html

[12] "Volcano/proton series 30a brushless esc." [Online]. Available: http://www.exceedrc.com/vose30abresc.html

[13] "Model psxxm / psxxl slide potentiometer." [Online]. Available: http://www.bitechnologies.com/products/slide_pots.htm

[14] "Ardupilot mega - arduino mega compatible uav controller." [Online]. Available: https://www.sparkfun.com/products/10294

[15] "Arduino board pro mini." [Online]. Available: http://arduino.cc/en/Main/Arduino-BoardProMini

[16] "Drv8835 dual motor driver carrier." [Online]. Available: http://www.pololu.com/cata-log/product/2135

[17] "R-78bxx-1.5 data sheet." [Online]. Available: http://www.recom-power.com/pdf/Innoline/R-78Bxx-1.5_L.pdf

[18] M. Agheli and S. Nestinger, "Lateral reachable workspace of axially symmetric mobile machining hexapod robots," in *Mechatronics and Embedded Systems and Applications (MESA), 2012 IEEE/ASME International Conference on*, 2012, pp. 81–86.

[19] J.-P. Merlet, C. M. Gosselin, and N. Mouly, "Workspaces of planar parallel manipulators," *Mechanism and Machine Theory*, vol. 33, no. 1C2, pp. 7 – 20, 1998.

[20] E. Macho, O. Altuzarra, C. Pinto, and A. Hernandez, "Workspaces associated to assembly modes of the 5r planar parallel manipulator," *Robotica*, vol. 26, pp. 395–403, 5 2008.

[21] X.-J. Liu, J. Wang, and G. Pritschow, "Kinematics, singularity and workspace of planar 5r symmetrical parallel mechanisms," *Mechanism and Machine Theory*, vol. 41, no. 2, pp. 145 – 169, 2006.

[22] J. J. Cervantes-Sanchez, J. C. Hernandez-Rodriguez, and J. Angeles, "On the kinematic design of the 5r planar, symmetric manipulator," *Mech. Mach. Theory*, vol. 36, no. 11, pp. 1303–1313, Nov 2001.

[23] J. J. Cervantes-Sanchez, J. C. Hernandez-Rodriguez, and J. G. Rendon-Sanchez, "On the workspace, assembly configurations and singularity curves of the rrrrr-type planar manipulator," *Mech. Mach. Theory*, vol. 35, no. 8, pp. 1117–1139, Aug 2000.

[24] C. M. Gosselin and M. Jean, "Determination of the workspace of planar parallel manipulators with joint limits," *Robotics and Autonomous Systems*, vol. 17, no. 3, pp. 129 – 138, 1996.

[25] H. Li, C. M. Gosselin, and M. J. Richard, “Determination of maximal singularity-free zones in the workspace of planar three-degree-of-freedom parallel mechanisms,” *Mechanism and Machine Theory*, vol. 41, no. 10, pp. 1157 – 1167, 2006.

[26] I. Ebrahimi, J. A. Carretero, and R. Boudreau, “3-prrr redundant planar parallel manipulator: Inverse displacement, workspace and singularity analyses,” *Mech. Mach. Theory*, vol. 42, no. 8, pp. 1007–1016, Aug 2007.

[27] X.-J. Liu, J.-S. Wang, and F. Gao, “On the optimum design of planar 3-dof parallel manipulators with respect to the workspace,” in *Robotics and Automation, 2000. Proceedings. ICRA ’00. IEEE International Conference on*, vol. 4, 2000, pp. 4122–4127 vol.4.

[28] S. V. Sreenivasan and B. H. Wilcox, “Stability and traction control of an actively actuated micro-rover,” *Journal of Robotic Systems*, vol. 11, no. 6, pp. 487–502, 1994. [Online]. Available: http://dx.doi.org/10.1002/rob.4620110604

[29] M. Agheli and S. Nestinger, “Study of the foot force stability margin for multi-legged/wheeled robots under dynamic situations,” in *Mechatronics and Embedded Systems and Applications (MESA), 2012 IEEE/ASME International Conference on*, 2012, pp. 99–104.

Compiled on Thursday 12th September, 2013